学位論文 （要約）

The last millennium precipitation in Japan reconstructed using oxygen isotopes from tree-rings

（樹木年輪の酸素同位体を用いた
過去 1000 年間の日本の降水量復元に関する研究）

平成 27 年 12 月博士（理学）申請
東京大学大学院理学系研究科
地球惑星科学専攻

坂下　渉

The last millennium precipitation in Japan reconstructed using oxygen isotopes from tree-rings

Wataru Sakashita

Department of Earth and Planetary Science, The University of Tokyo

Abstract

The Asian monsoon, characterized by variations of the strength and expansion of the summer rain band, is an important part of the Earth's climate system. The long-term hydrological conditions in East Asia indicate complicated rainfall pattern during the last millennium. Previous works proposed that the El Niño-like and La Niña-like equatorial Pacific conditions had an important role for controlling precipitation in East China and its surroundings. To develop the understanding of physical processes in the western North Pacific, hydrological reconstructions are needed in Japan. However, there are as of now few studies that reconstructed the hydrological variability in this region.

The main research objective of this thesis is the annually resolved reconstructions of past hydroclimate changes in Japan. To reconstruct the long-term hydrological condition, I focus on tree-ring cellulose oxygen isotopes ($\delta^{18}O$) from cedar trees in Japan. In chapter 2, two long cedar tree-ring cellulose $\delta^{18}O$ from central Japan are presented during the past four centuries. These data allow me to consider that cedar trees from Japan are suitable to reconstruct the long-term hydroclimate variability. In chapter 3, I report another cedar $\delta^{18}O$ chronology in Yakushima Island from the Medieval Climate Anomaly (MCA) and Little Ice Age (LIA). In this chapter, tree-ring growth rate and meteorological conditions are also observed in Yakushima Island. Based on these reconstructions, I discuss about the possible influence of the Pacific Sea Surface Temperature (SST) on the long-term hydrological variations in central Japan (Chapter 4) and Yakushima Island (Chapter 5). These discussions indicate that the equatorial Pacific SST and the Kuroshio Current play important roles in the hydrological conditions in central Japan and Yakushima Island, respectively. In Chapter 6, I investigate relationships between El Niño–Southern Oscillation (ENSO) and tree-ring cellulose $\delta^{18}O$. In the final chapter, I provide the general discussion and future perspectives of this thesis (Chapter 7). This discussion can develop an understanding of the mechanism for the long-term rainfall pattern in eastern part of East Asia. Key findings in each chapter are summarized in the followings.

Tree-ring cellulose oxygen isotopes in central Japan (Chapter 2): Measurements of cellulose $\delta^{18}O$ were performed for two long cedar trees from central Japan. These two chronologies allowed me to consider the age-related trend of Japanese cedars from

central Japan. Results indicated that Mie tree-ring cellulose $\delta^{18}O$ significantly correlated with May–June–July (MJJ) relative humidity. Time-domain comparisons using two long chronologies showed that these data were consistent throughout the majority of the past four centuries, except for the end of 18th century. Regression lines for tree-ring $\delta^{18}O$ indicated that there were no significant age-related trends in cedar trees from central Japan, except for the $\delta^{18}O$ values of inner cedar.

Tree-ring cellulose oxygen isotopes in Yakushima Island (Chapter 3): I measured Yakushima tree-ring cellulose $\delta^{18}O$ from the MCA and LIA. Results showed that there were no significant correlations between the tree-ring cellulose $\delta^{18}O$ and relative humidity, suggesting that this proxy was mainly controlled by the source water $\delta^{18}O$ changes. Assuming that the source water $\delta^{18}O$ variations mainly controlled by the amount effect, further correlation analysis was performed for precipitation data. This analysis indicated that Yakushima tree-ring cellulose $\delta^{18}O$ significantly correlated with May–June (MJ) precipitation. Meteorological data and tree-ring growth observations supported this correlation.

Relative humidity reconstruction in central Japan during the Little Ice Age (Chapter 4): Here, I reconstructed the variations of hydrological condition in the Meiyu/Baiu season from AD 1600–1959 by using tree-ring cellulose $\delta^{18}O$ from central Japan. Data suggested that the wettest period occurred around AD 1790–1860, the final stage of the LIA. Comparisons between this relative humidity reconstruction and global SSTs suggested that SST variability in the equatorial Pacific played an important role in the hydrological conditions of central Japan.

Hydroclimate reconstruction in Yakushima Island over the past millennium (Chapter 5): Here I presented a tree-ring cellulose $\delta^{18}O$ chronology for Yakushima Island from AD 1025 to 1805. Assuming that this data mainly controlled by the amount effect, the results indicated that precipitation decreased during the LIA relative to the MCA. Meteorological precipitation data and tree-ring cellulose $\delta^{18}O$ synchronized with SST variations around the western North Pacific, suggesting that the Kuroshio Current played an important role in this hydroclimate changes.

Relationship between tree-ring cellulose oxygen isotopes in Japan and the El Niño–Southern Oscillation (Chapter 6): The ENSO is known to strongly influence East Asian Summer Monsoon (EASM) rainfall in the present-day climate, but the relatively

short instrumental rainfall record hindered the development of a longer-term understanding of this teleconnection. To overcome this issue, here I presented tree-ring cellulose $\delta^{18}O$ from AD 1612 to 1935. Time- and frequency-domain comparison of the tree-ring $\delta^{18}O$ record and recent ENSO reconstructions revealed a common high-frequency (3–8 year) variability that characterized the mid-17th, late 18th and late 19th centuries. Similar analyses of instrumental MJ precipitation and several ENSO indexes during the 20th century indicated that this high-frequency oscillation reappeared from AD 1980. In addition, comparison of ENSO and Pacific Decadal Oscillation (PDO) indexes indicated that the ENSO-EASM teleconnection was strong when ENSO variance was high, and the PDO phase may relate to the ENSO-EASM relationship over the past 400 years.

Contents

Abstract

Chapter 1

Chapter 1

General Introduction

1-1. Paleoclimate over the past millennium

1-1-1. Little Ice Age and Medieval Climate Anomaly

The Little Ice Age (LIA) and the Medieval Climate Anomaly (MCA) are the most recent periods of naturally induced global climate changes, and events during these times have been a focus of many studies (e.g., Mann, 2002; Mann et al., 2009). These periods are thought to be of great importance for understanding responses of the climate system to volcanic and solar forcing (e.g., Mann et al., 1998; Masson-Delmotte et al., 2013).

Previous studies mainly focused on temperature reconstructions, and the data show that many regions around the world experienced a cold climate from about AD 1450 to 1850 and warm conditions from about AD 950 to 1250 (e.g., Masson-Delmotte et al., 2013) (Fig. 1-1-1). In these reconstructions, various climate proxies (e.g., tree-ring growth width, marine sediment, speleothem, ice core, coral, historical document) were used to reconstruct the temperature variations (e.g., Mann et al., 1998; Mann et al., 2008). Reconstructed Northern Hemisphere (NH) temperature anomalies from various climate archives show decreases of about 0.5 °C during the LIA and increases of about 0.7–1.3 °C during the MCA (e.g., Mann et al., 2009; Masson-Delmotte et al., 2013) (Fig. 1-1-1). Computer simulated temperatures during the LIA and MCA also showed about 0.3 °C decrease and increase, respectively (e.g., Masson-Delmotte et al., 2013) (Fig. 1-1-1).

Mann et al. (2009) reported that the reconstructed surface temperature pattern for the LIA and MCA. During the LIA, many regions around the world experienced a cold climate except for off southern Greenland (Fig. 1-1-2). This spatial temperature reconstruction also indicated that the temperature around the North Atlantic increased during the MCA (Fig. 1-1-2). These characteristics mean that the temperature changed widely over the past millennium.

1-1-2. The past millennium climate during the Holocene

In this section, I briefly review climate changes since glacial periods and

summarize an importance of the past millennium climate variations during the Holocene. Previous works identified that global climates have experienced the glacial–interglacial cycles during the past 300 kyr (e.g, Kawamura et al., 2007). Ice core oxygen isotopes (δ^{18}O) from Dome Fuji showed that the reconstructed temperature had glacial–interglacial cycles, which were synchronized with orbital insolation variability (e.g, Kawamura et al., 2007; Fig. 1-1-3). The temperature deviation increased after the Last Glacial Maximum (LGM) around 20 kyr, and then, it reached the maximum around 10kyr. This interglacial state has continued to the present (Holocene).

While the amplitudes of this climate variability are relatively small in the past 300 kyr, there are important climate variations during this period. Globally stacked temperature reconstruction for the Holocene showed that global climate experienced a warm period from about 9500 to 5500 year BP (Holocene thermal maximum) (Marcott et al., 2013; Fig. 1-1-4). This warm climate shifted to cooler conditions and this temperature decrease was synchronized with the orbital insolation variability (e.g., Wanner et al., 2008). The temperature anomaly reached the minimum around the LIA, and then, the climate shifted to present warm conditions. Thus, the LIA is the naturally induced coldest period over the past 10,000 years. The amplitude of deference between the cold (LIA) and warm periods (MCA, 20 century) is relatively large during the Holocene. These characteristics allow me to constrain responses of climate system to natural radiative forcing.

インターネット公表に関する同意が
得られなかったため非公表

Fig. 1-1-1. Comparison of reconstructed and simulated NH temperature anomalies over the last millennium (modified from Masson-Delmotte et al., 2013). These temperatures represent anomalies from their AD 1500–1850 averages. Grey shading shows reconstructed temperature. Simulated temperatures are shown by colored lines. Thick red (blue) line indicates the strong (weak) solar variability simulations. Thin red and blue lines show multi-model 90% range. Medieval Climate Anomaly, MCA; Little Ice Age, LIA; 20th century, 20C.

インターネット公表に関する同意が
得られなかったため非公表

Fig. 1-1-2. Spatial temperature pattern for MCA and LIA (Mann et al., 2009). Temperature anomalies show difference from the mean of reference period (AD 1961–1990).

インターネット公表に関する同意が
得られなかったため非公表

Fig. 1-1-3. Comparison of Dome Fuji climate and insolation (modified from Kawamura et al., 2007). Black and red lines indicate Dome Fuji $\delta^{18}O$ (Watanabe et al., 2003) and temperature deviation from the mean of the last 10 kyr, respectively. Orange (light blue dashed) line indicates summer solstice insolation at 65ºN (65ºS).

インターネット公表に関する同意が
得られなかったため非公表

Fig. 1-1-4. Globally stacked temperature for the Holocene and the last two millennia (modified from Marcott et al., 2013). Purple line indicates the 5º grid area-weighted mean of the 73 records with 1σ uncertainty (blue band). Dark gray line shows the global mean temperature of Mann et al. (2008) with their uncertainty (light gray band).

1-2. Long-term climate variation and rainfall pattern in Asia

The Asian summer monsoon transports large quantities of water to the continent of Asia and is an important component of the global atmospheric circulation system. Understanding spatio-temporal changes and patterns in precipitation is a major challenge in climate sciences, and these types of data are necessary to better project future climate changes (IPCC, 2013).

1-2-1. Atmospheric circulation and rainfall pattern in Asia

In this section, I summarize the atmospheric circulation and rainfall pattern in Asia (Ogura, 1999). The average July global precipitation for AD 1988–1996 shows that the rain band is found along the latitude of 10°N (Fig. 1-2-1). This area is called the Inter Tropical Convergence Zone (ITCZ). In the equatorial region, trade winds of both northern and southern hemispheres converge on the latitude of 10°N, and then, an updraft occurs in this area. This updraft reaches the tropopause, and the branched currents decline around 30°N and 30°S (Fig. 1-2-2). This atmospheric circulation is called the Hadley circulation. In the mid-latitude, the average July precipitation shows less rainfall because of the downdraft of Hadley circulation (Fig. 1-2-1).

Equatorial regions also have the atmospheric circulation of east-west direction called the Walker circulation. In the neutral conditions, an updraft occurs in the western equatorial Pacific because of high sea surface temperature (SST) in this area (Fig. 1-2-3). This air current reaches the tropopause, and then, declines around the eastern equatorial Pacific. This atmospheric circulation plays an important role in the El Niño–Southern Oscillation (ENSO).

Summer monsoon transports large quantities of water to the continent and is an important component of the global atmospheric circulation system. This phenomenon is basically caused by thermal differences between continent and ocean, and the Indian and East Asian summer monsoons are the main subsystem in Asia (Fig. 1-2-4).

The average July global rainfall shows that the Meiyu/Baiu rain band is found around Japanese region (Fig. 1-2-1). In this phenomenon, Tibetan Plateau plays an

6

important role in the rain band formation. This is because the high altitudes (an average elevation of 5,000 m) hinder the progress of the Indian summer monsoon. This advances to the East Asia, and then, the wet and warm monsoon meet the relatively dry and cool westerlies around Japan. The Meiyu/Baiu rain band is caused by these large differences of water vapor and potential temperature between summer monsoon and westerlies.

インターネット公表に関する同意が
得られなかったため非公表

Fig. 1-2-1. Average July global precipitation for AD 1988–1996 (http://www-das.uwyo.edu/~geerts/cwx/notes/chap10/global_precip.html).

インターネット公表に関する同意が

得られなかったため非公表

Fig. 1-2-2. Schematic diagram of the Hadley circulation (from NOAA website: https://www.climate.gov/news-features/blogs/enso/how-enso-leads-cascade-global-impacts).

インターネット公表に関する同意が

得られなかったため非公表

Fig.1-2-3. Schematic diagram of the Walker circulation (from NOAA website: https://www.climate.gov/news-features/blogs/enso/walker-circulation-ensos-atmospheric-buddy).

インターネット公表に関する同意が
得られなかったため非公表

Fig.1-2-4. Map showing two main subsystem (Indian summer monsoon and East Asian summer monsoon) of the Asian monsoon (Li et al., 2014; modified from Wang and Lin, 2002).

During the Meiyu-Baiu season, the precipitation variations in East Asia are influenced by many factors. Here I summarize the phenomenon, which potentially affects the early summer rainfall in this region.

Previous studies have identified the ENSO as a potential important factor for the East Asian summer monsoon (EASM) (e.g., Wang et al., 2000; Wu and Wang, 2002). A schematic diagram of El Niño is shown in Fig. 1-2-5. In the El Niño condition, the SST anomalies in the western (middle and eastern) equatorial Pacific exhibit negative (positive). These SST patterns change the thermocline gradient (Fig. 1-2-5), and the precipitation in the western equatorial Pacific (e.g., Indonesia) decrease during the El Niño. In the La Niña condition, inverse phenomenon occurs in the equatorial pacific. This phenomenon at low latitude can influence on the mid latitude climate by teleconnections.

In the western Pacific, Pacific Japan pattern (PJ pattern) influences on the inter-annual climate variations in Japan during the summer season (Nitta, 1987). In the positive (negative) phase of the PJ pattern, the positive (negative) anomalies of SST around the Philippines lead to an active (inactive) western Pacific subtropical high because meridional atmospheric circulation in the western North Pacific is active (inactive) and the downdraft around Japan is strong (weak) (Fig 1-2-6). This teleconnection pattern is a primary control factor of inter-annual variability for the EASM (Nitta, 1987). Kubota et al. (2015) has presented a 117-year PJ pattern index using station pressure data from AD 1897 to 2013. This long index revealed that the relation between ENSO and PJ pattern has inter-decadal variability. Significant correlations are exhibited in the beginning of the 20th century and 1930s, whereas there are low correlations in the 1920s and from the 1940s to 1970s (Fig. 1-2-7) (Kubota et al., 2015). This inter-decadal modulation suggests that the influence of PJ variability changed over the past 117 years.

Previous works reported that decadal changes of the Kuroshio Current also significantly affect the early summer rainfall in East Asia (Tomita et al., 2007). The Kuroshio Current transports the large amount of heat flux from the ocean to the continent, the typical paths are shown in Fig. 1-2-8 (Kawabe, 1995). The heat flux of Kuroshio region changed around AD 1990 (Fig. 1-2-9). The atmospheric circulation synchronized with this decadal change, and the sea level pressure anomalies had meridional dipole pattern in the northwestern Pacific (Fig. 1-2-10) (Tomita et al., 2007).

This decadal variation significantly affects the increase of June precipitation over the area around the Southeast China and western Japan (Fig. 1-2-11) (Tomita et al., 2007).

インターネット公表に関する同意が
得られなかったため非公表

Fig. 1-2-5. A Schematic diagram of El Niño conditions (from NOAA website: http://www.pmel.noaa.gov/tao/elnino/.noaa/enso.html).

インターネット公表に関する同意が
得られなかったため非公表

Fig. 1-2-6. Pattern of sea level pressure anomalies in the western Pacific (Kubota et al., 2015). Contours indicate the sea level pressure anomalies in JJA for 1979–2009, which are drawn for ±0.1, ±0.3, ±0.5, … hPa. Coloring indicates correlations with respect to leading principle component of 850 hPa vorticity over (10° –55°N, 100° –160°E). Stippling represents the 95% confidence level.

インターネット公表に関する同意が
得られなかったため非公表

Fig. 1-2-7. 21-year running correlations of the 117-year PJ index with Southern Oscillation Index (SOI) (black line) and Niño 3.4 SST (purple line) (Kubota et al., 2015). Dashed lines represents the 95% confidence level.

インターネット公表に関する同意が
得られなかったため非公表

Fig. 1-2-8. Typical paths of the Kuroshio Current (Kawabe, 1995).

インターネット公表に関する同意が
得られなかったため非公表

Fig. 1-2-9. Differences between 1990s and 1980s for sea surface heat flux in June (Tomita et al., 2007). Contours are drawn with 10 W/m^2 intervals, and shading represents the 95% confidence level.

インターネット公表に関する同意が
得られなかったため非公表

Fig. 1-2-10. Differences between 1990s and 1980s for atmospheric circulation in June (Tomita et al., 2007). Contours indicate the anomalies of sea level pressure, which are drawn for every 0.25 hPa. Dot-lines are negative anomalies of sea level pressure. Shading represents the 95% confidence level. Arrows show the surface winds.

インターネット公表に関する同意が
得られなかったため非公表

Fig. 1-2-11. Differences between 1990s and 1980s for June precipitation (Tomita et al., 2007). Contours are drawn with 30 mm/month interval. Dot-lines are negative anomalies of precipitation. Shading represents the 95% confidence level.

1-2-2. Long-term changes of rainfall pattern in Asia

In this section, I summarize the rainfall patterns over the past millennium in the western equatorial Pacific regions, China and Japan. Longer-term paleoclimate records show strong correlations between NH temperatures and precipitation in Asia (e.g., Wang et al., 2001; Yokoyama et al., 2006; Nakamura et al., 2015). During the LIA, precipitation decreases in simulated global monsoon have been observed (e.g., Liu et al., 2009; Masson-Delmotte et al., 2013), whereas proxy-based rainfall reconstructions indicate that regional precipitation patterns are complicated in that they are not simply correlated with temperature as described below.

Western equatorial Pacific regions

In the western equatorial Pacific regions, hydrological reconstructions over the past millennium have been presented (reviewed by Yan et al. (2015)). The fluvial sediment records from Northwestern Australia suggest a dry condition in this area (D11 and D12 in Fig. 1-2-12) during the LIA (Wasson et al., 2010). A similar characteristic also was observed in the stalagmite record from the same area (D13 in Fig. 1-2-12; Denniston et al., 2013). In contrast, the precipitation around the Indo-Pacific Warm Pool region increased during the LIA relative to MCA/the past 150 years (Yan et al., 2015). Organic matter stable carbon isotopes (δ^{13}C) of lake sediment from Java (W3 in Fig. 1-2-12; Rodysill et al., 2013) indicate a wetter condition during the LIA. The hydrological reconstructions using a leaf wax hydrogen isotopes (δD) from Makassar Strait (W4 in Fig. 1-2-12; Tierney et al., 2010) and the δ^{18}O and Mg/Ca of planktonic foraminifera from the same area (W5 in Fig. 1-2-12; Oppo et al., 2009) are consistent with the rainfall increase during this period. Yan et al. (2015) proposed this rainfall pattern indicated the weakened Australian Summer Monsoon (ASM) during the LIA.

インターネット公表に関する同意が
得られなかったため非公表

Fig. 1-2-12. Australian Summer Monsoon (ASM) rainfall pattern during the LIA (Yan et al., 2015). Coloring indicates average summer precipitation (December–February) in the ASM. This mean precipitation is derived from NCEP reanalysis2 from January 1979 to December 2010. This map also shows the locations of proxy-based hydrology reconstructions (upward triangle: lake or marine sediment; circle: stalagmite; cross symbol: coral). The temporal hydrological variations over the past millennium are also shown in the figure (W4: Tierney et al., 2010; W5: Oppo et al., 2009; D11: Wasson et al., 2010; D13: Denniston et al., 2013).

China

Hydrological reconstructions in China showed the regional difference of rainfall pattern over the past millennium (reviewed by Yan et al., 2015). In the northern limit of the EASM, some hydrological proxies (a lake sediment, a historical archive and two stalagmite records) indicated a dry condition during the LIA relative to the MCA and the past 150 years (from D1 to D4 areas in Fig. 1-2-13; Tan et al., 2010; Zhang et al., 2008; Hu et al., 2008; Liu et al., 2011b; Tan et al., 2008). The opposite hydrological patterns were observed in the southern coast of China and northern South China Sea (W1 and W2 in Fig. 1-2-13; Yan et al., 2011; Chu et al., 2002; Zeng et al., 2011). A moderate drought during the LIA was observed between the North and South China (e.g., N2 in Fig. 1-2-13; Qin et al., 2008). Yan et al. (2015) suggested that these rainfall patterns indicate a retreat of EASM during the LIA. They summarized the spatial rainfall variations in East Asia-Australia areas during the LIA (Fig. 1-2-14), and hypothesized a contraction of the monsoon and ITCZ zone over this period (Yan et al., 2015).

On the other hand, further compilations of hydrological reconstructions in eastern China may indicate that the atmospheric circulation is more complicated than the hypothesized circulation change of Yan et al. (2015). Zhou et al. (2011) investigated the rainfall pattern changes in eastern China on centennial time scale. This analysis suggested that the Asian summer monsoon was the strongest (weakest) during the late MCA (early LIA) over the last millennium. The rainfall pattern indicated that flood (drought) occurred in the Yellow River Catchment and drought (flood) was exhibited in the Yangtze River Catchment during the late MCA (early LIA). Chen et al. (2015) proposed that this "north–south" mode of precipitation dominated the precipitation in eastern China during not only the last millennium (Fig. 1-2-15) but also the modern period (Fig. 1-2-16).

The possible mechanisms of this rainfall pattern are proposed in Chen et al. (2015). The intensity and position of Western Pacific Subtropical High (WPSH) potentially play an important role in modulating relations between precipitation in eastern China and ENSO. In the El Niño years, westward intensification and extension were observed in the WPSH, and this also shifted southward (Qian et al., 2007; Su and

Xue, 2011). During this state, the rain-belt is not able to reach to North China relative to neutral years. This can cause more precipitation in southern China (e.g., lower Yangtze River Catchment) and less rainfall in northern China. In La Niña years, intensity and position of the WPSH indicated weak and northeastwards retreat due to smooth transports of moisture by low-level jet along the northwestern edge of the WPSH (Zhou and Yu, 2005). On multi-centennial timescales, the similar patterns were observed in the reconstructed hydrological conditions during the last millennium (Fig. 1-2-15). Some previous studies have identified that equatorial Pacific Ocean had La Niña (El Niño) like condition in the MCA (LIA) (e.g., Mann et al., 2009). This La Niña-like condition would lead to more precipitation in northern China and less precipitation in southern China. During the LIA, opposite rainfall patterns were observed causing by El Niño-like condition. However, as of now, there are not enough proxy records in eastern China and its surroundings to discuss about this asynchronous variability (Chen et al., 2015).

インターネット公表に関する同意が
得られなかったため非公表

Fig. 1-2-13. East Asian Summer Monsoon (EASM) rainfall pattern during the LIA (Yan et al., 2015). Coloring indicates average summer precipitation (June–October) in the EASM. This mean precipitation is derived from NCEP reanalysis2 from January 1979 to December 2010. This map also shows the locations of proxy-based hydrology reconstructions (upward triangle: lake or marine sediment; square: historic archive; circle: stalagmite). The temporal hydrological variations over the past millennium are also shown in the figure (W2: Yan et al., 2011; N2: Qin et al., 2008; D4: Zhang et al., 2008).

Fig. 1-2-14. Schematic map indicating the modern limit of monsoon in the East Asia–Australia area, and the hypothesized limits of monsoon zone during the LIA (Yan et al., 2015). Pink solid represents current limits of EASM and ASM. Red (Blue) shadings indicate the dry (wet) areas during the LIA relative to the MCA and the past 150 years.

インターネット公表に関する同意が
得られなかったため非公表

Fig. 1-2-15. Map showing the hydrological conditions during the MCA and LIA (Chen et al., 2015). Proxy-based wetness was classified into dry, moderate and wet. Minus and plus symbols indicate the moderately dry and moderately wet, respectively.

インターネット公表に関する同意が
得られなかったため非公表

Fig. 1-2-16. EOF1 pattern based on the annual precipitation during the AD 1900–2008 (Chen et al., 2015). The values indicate the eigenvectors of EOF1 mode.

Japan

Previous studies reported temperature reconstructions using various climate archives, but there are still few reconstructions of hydrological condition in Japan during the last millennium. Here, I summarize the previous works of climate reconstructions in Japan during this period.

Reconstructions using documentary records and tree-ring width chronologies are successful to provide the past temperature changes in Japan. Spring temperature in Kyoto was reconstructed using the phonological data for cherry tree since 9th century, and the results showed some cold periods (Aono and Kazui, 2008). Tree-ring widths chronologies from central and northeast Japan also provided the spring temperatures over the past 300 years (Yonenobu and Eckstein, 2006; Ohyama et al., 2013).

On the other hand, hydrological reconstructions are extremely sparse in and around Japan during the last millennium. A previous study reconstructed the precipitation frequency from AD 1661 to 1868 in this area by using historical documents from northern Japan (Maejima and Tagami, 1983). This climate reconstruction using daily weather records reported some climate phases, but temporal changes of precipitation are still unclear. Sun et al. (2015) present regional hydroclimate reconstruction in Northern Japan during the past 400 years. Their sediment core nitrogen isotopes (δ^{15}N) record from Lake Onuma revealed the long-term hydrological variability in Hokkaido. However, there are still no hydroclimate reconstructions using lake sediment core in central and southern Japan during the last millennium. While tree-ring width chronologies may be an excellent archive of monsoon history during the last millennium, records from Japan are not only extremely sparse (Fig. 1-2-17; Cook et al. 2010), but also generally reflective of temperature, rather than precipitation (e.g., Yonenobu and Eckstein, 2006).

インターネット公表に関する同意が
得られなかったため非公表

Fig. 1-2-17. (A) Map showing the monsoon over Africa, India, East Asia and northern Australia (Cook et al., 2010). (B) 327-series tree-ring chronology network (green dots) with the 534 grid points of instrumental Palmer Drought Severity Index (PDSI).

1-2-3. Modeling of rainfall pattern

In previous studies, East Asian monsoon rainfall was simulated with various models, including the Max Planck Institute Earth System Model (MPI-ESM), (Man et al., 2012; Yan et al., 2015), the Flexible Global Ocean–Atmosphere–Land–Sea ice (FGOALS) model (Zhou et al., 2011), and the ECHO-G model (Liu et al., 2009; Liu et al., 2011a). In this section, we summarize the model performance in East Asia over the last millennium.

Validations of the model performances indicate that the some models are not able to well reproduce the present-day monsoon rain band from eastern China to Japan. Comparison between observed and simulated precipitation using MPI-ESM showed the similar rainfall pattern around the Japanese region (Fig. 1-2-18ab; Man et al., 2012). In the FGOALS model, some discrepancies (e.g., central China) are exhibited in the validation of model performance (Fig. 1-2-19ab; Zhou et al., 2011). The simulated seasonal cycles of extra tropical and subtropical East Asia in the MPI-ESM model well reproduced temporal precipitation variations (Fig. 1-2-18cd; Man et al., 2012). The monthly variability using FGOALS model indicates that the precipitation peaks were a lag of about 1–3 month compared to observations (Fig. 1-2-19cd; Zhou et al., 2011). Thus, MPI-ESM model reproduced the precipitation in East Asia more accurate than FGOALS model.

Simulated rainfall patterns over the past millennium were also performed by these climate models. In the model of Liu et al. (2009) and Zhou et al. (2011), they considered solar variability, volcanic activity, and greenhouse gases as external explanatory factors. Man et al. (2012) used land cover change along with these three external factors. Yan et al. (2015) presented simulated precipitation using only total solar irradiance (TSI) as an external forcing. In and around Japan, the simulated rainfall patterns mostly showed wet conditions during the MCA relative to LIA (Fig. 1-2-21; Zhou et al., 2011), except for the results of Man et al. (2012) (Fig. 1-2-20).

Fig. 1-2-18. Validation of the performance using MPI-ESM model (Man et al., 2012). (a) Observed mean summer (JJA) precipitation of CMAP and 850-hPa wind of NCEP2. Units of coloring and arrow are mm/day and m/s respectively. (b) Simulated rainfall pattern in East Asia. (c) and (d) Comparison of seasonal variations between the observed and simulated precipitation in northern East Asia (c) 36°–50°N, 100°–120°E; (d) 21°–35°N, 100°–120°E). All the data in figures are average values from AD 1979 to 2005.

Fig. 1-2-19. Validation of the performance using FGOALS model (Zhou et al., 2011). (a) Observed mean annual precipitation of CMAP. (b) Simulated rainfall pattern in East Asia. (c) and (d) Comparison of seasonal variations between the observed and simulated precipitation in northern East Asia (c) 36°–50°N, 100°–120°E; (d) 21°–35°N, 100°–120°E). All the data in figures are average values from AD 1979 to 2005.

インターネット公表に関する同意が

得られなかったため非公表

Fig. 1-2-20. Differences of mean summer precipitation and 850-hPa wind between MWP (same as MCA) and LIA (Man et al., 2012). Units of coloring and arrow are mm/day and m/s respectively. Stippling indicates the 95% significant area.

Fig. 1-2-21. The EASM model showing precipitation differences between the MWP (same as MCA) and LIA (Zhou et al., 2011). Units of coloring and arrow are mm/day and m/s respectively.

Discrepancies between climate models have been also observed in the projecting rainfall change. IPCC Fifth Assessment Report (AR5) showed comparisons of estimated average seasonal precipitation patterns (IPCC, 2013). These are applied for the Representative Concentration Pathways (RCP) 8.5 scenarios. This scenario defines that radiative forcing at the end of the 21st century increases 8.5 W/m^2 relative to the Preindustrial period. Coupled Model Intercomparison Project Phase 5 (CMIP5) presented the averaged percentage changes in mean spring and summer precipitation compared to AD 1986 to 2005 average (Fig. 1-2-22 and Fig. 1-2-23). This indicates that the projected precipitation patterns have discrepancies between models (Collins et al., 2013). These differences are much larger than temperature predictions. In East Asia, the average percentage change in mean spring (March–April–May; MAM) precipitation over the AD 2045–2065 are mainly less than one standard deviation, indicating that the agreements with models are less than 66% (Fig. 1-2-22). During the summer season (June–July–August; JJA), only a few areas agree with the 90% of the results from the models (Fig. 1-2-23).

Fig. 1-2-22. CMIP5 average percentage change in mean spring (MAM) precipitation during the period from AD 2045 to 2065 under the RCP8.5 forcing scenario (IPCC, 2013). The reference period is from AD 1986 to 2005. Hatching regions show that the mean change of multi-model is less than one standard deviation. Stippling indicates areas where more than 90% of the models agree on.

Fig. 1-2-23. Same as Fig 1-2-22, except for mean summer (JJA) precipitation (IPCC, 2013).

1-2-4. Oxygen isotope theory

To reconstruct long-term hydrological conditions in Japan, I focused on tree-ring cellulose $\delta^{18}O$. This proxy enables reconstruction of paleoclimates at annual resolution while tree-rings grow. The developments of reconstructions using this tool are divided into some phases (reviewed by Sternberg, 2009). First, Libby et al. (1976) identified that the tree-ring cellulose $\delta^{18}O$ datasets of German oak trees correlate to the temperature variations. Previous studies reported that these tree-ring data could be used as temperature, relative humidity and precipitation proxies (e.g., Burk and Stuiver, 1981; Ramesh et al., 1986). However, these reconstructions were based on an empirical relationship between tree-ring cellulose $\delta^{18}O$ and meteorological data. Thus, at that point, tree-ring cellulose $\delta^{18}O$ was not a robust paleoclimate proxy, which is not affected by taxa and/or locations. In the second phase, the tree-ring cellulose $\delta^{18}O$ model was proposed by Roden et al. (2000), and this study increased a reliability of tree-ring cellulose $\delta^{18}O$ as it helped us understand physiological and biochemical mechanisms of this proxy.

Here I describe the oxygen isotope theory of tree-ring cellulose (reviewed by Sano et al., 2012). Previous studies have confirmed that there is no isotopic fractionation when trees take up water in soil through their roots (e.g., White et al., 1985). This water is transported to leaves through xylem. In leaves, oxygen isotopes ($\delta^{18}O_{leaf}$) are controlled by transpiration through stomata. The modified Craig–Gordon equation (Craig and Gordon, 1965) describe this process as:

$$\delta^{18}O_{leaf} = \delta^{18}O_x + \varepsilon^* + \varepsilon_k + e_a/e_i \, (\delta^{18}O_a - \varepsilon_k - \delta^{18}O_x) \qquad \text{(Eq. 1)}$$

e_a/e_i indicates the ratio of ambient vapor pressure to the one inside the leaf. $\delta^{18}O_a$ and $\delta^{18}O_x$ are the $\delta^{18}O$ values of atmospheric vapor and stem water, respectively. Equilibrium and kinetic isotopic fractionation factors are expressed as ε^* and ε_k, respectively. Tree-ring oxygen isotope model regards the oxygen isotopes of stem water ($\delta^{18}O_x$) as that of precipitation ($\delta^{18}O_p$), and the ratio of ambient vapor pressure (e_a/e_i) is also considered to the relative humidity (h) (Dongmann et al., 1974). In this model, the

atmospheric vapor is isotopically equilibrated with precipitation ($\delta^{18}O_a = \delta^{18}O_p - \varepsilon^*$). Therefore, the modified Craig–Gordon equation (Eq. 1) can be expressed as

$$\delta^{18}O_{leaf} = \delta^{18}O_p + (\varepsilon^* + \varepsilon_k)(1-h) \qquad (Eq.\ 2)$$

Previous studies reported that the equilibrium isotopic fractionation factor (ε^*) is 9.8‰ at 20 °C (Majoube, 1971) and the ε_k can be considered as about 26.5‰ (Farquhar et al., 1989). This simplified equation indicates that $\delta^{18}O_{leaf}$ is mainly controlled by the oxygen isotopes of precipitation ($\delta^{18}O_p$) and relative humidity (Fig. 1-2-24).

Biochemical fractionation of the sucrose synthesis also affects the oxygen isotopes of cellulose ($\delta^{18}O_c$). Previous works (Roden et al., 2000; Sternberg, 2009) showed $\delta^{18}O_c$ as

$$\delta^{18}O_c = f(\delta^{18}O_x + \varepsilon_0) + (1-f)(\delta^{18}O_{leaf} + 27‰) \qquad (Eq.\ 3)$$

f is the ratio of oxygen that exchange with xylem water (precipitation), ε_0 is the isotopic fractionation factor between exchanged oxygen from carbohydrate and xylem water during cellulose synthesis. Oxygen isotope fractionation for the exchangeable oxygen in sucrose is assumed to 27‰ relative to leaf water (Roden et al., 2000; Sternberg, 2009). Roden et al. (2000) estimated that the above proportion (f) is 0.42 for $\varepsilon_0 = 27‰$. Therefore, this oxygen isotope theory suggests that oxygen isotopes of cellulose are mainly controlled by the two factors (oxygen isotopes of precipitation ($\delta^{18}O_p$) and relative humidity).

$H_2O_{vapor\text{-}out}$ $(\delta^{18}O_a)$

Isotopic fractionation: ε_k F2   F3

Mass balance equation

F1 + F2 = F3

$H_2O_{vapor\text{-}in}$

Isotopic balance equation

Isotopic fractionation: ε^*

$\delta^{18}O_x \times F1 + (\delta^{18}O_a - \varepsilon_k) \times F2 =$

$(\delta^{18}O_{leaf} - \varepsilon^* - \varepsilon_k) \times F3$

H_2O_{in} $(\delta^{18}O_{leaf})$

some assumptions... (details in the manuscript)

F1 $(\delta^{18}O_x)$

$\delta^{18}O_{leaf} = \delta^{18}O_x + (\varepsilon^* + \varepsilon_k)\,(1-h)$
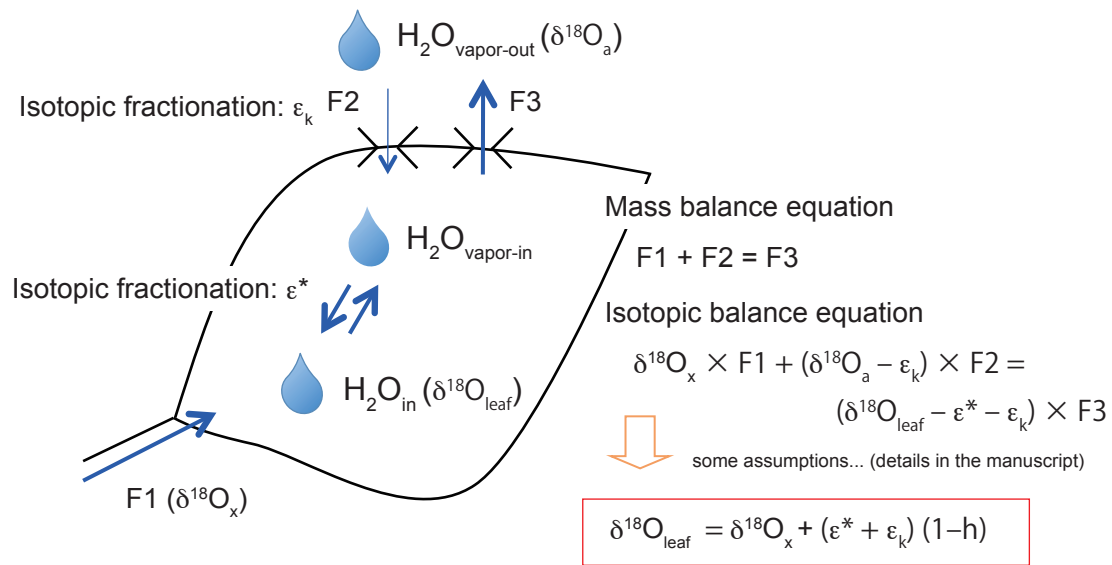
Fig. 1-2-24. Tree-ring oxygen isotope model (modified from Nakatsuka, 2007).

1-2-5. Long-term hydroclimate reconstructions using tree-ring cellulose δ^{18}O

Tree-ring cellulose δ^{18}O allows for successful hydroclimate reconstructions at multiple East Asia locations. In Southeast Asia, Sano et al. (2012) reported 300-year tree-ring cellulose δ^{18}O chronologies (AD 1705–2004) using 6 cypress trees from northern Vietnam (Fig. 1-2-25). Tree-ring cellulose δ^{18}O chronologies were also presented in northern Laos from AD 1588 to 2002 (Xu et al., 2013). Comparison of these datasets showed significant positive correlation (r = 0.70; p < 0.001; n =298), indicating that regional hydrological variations in Southeast Asia are well recorded in tree-ring cellulose δ^{18}O data (Sano et al., 2012; Xu et al., 2013; Fig. 1-2-26).

Previous studies examined main factor of tree-ring cellulose δ^{18}O in Japan. Nakatsuka et al. (2004) presented tree-ring cellulose δ^{18}O and δ^{13}C for 5 oak and 4 fir trees in northern Japan. Comparisons of these datasets revealed that tree-ring cellulose δ^{18}O from same area showed similar temporal variations, whereas that of δ^{13}C had some discrepancies (Fig. 1-2-27). These differences may relate to ecological effects (e.g., competition for light with neighboring trees). Thus, the tree-ring δ^{18}O from northern Japan well recorded past hydroclimate variations regardless of species. In central Japan, Yamaguchi et al. (2010) reported two tree-ring cellulose δ^{18}O chronologies from Nara cedar (34°32'N, 136°02'E, 405 m a.s.l.) and Shiga cypress (34°55'N, 135°59'E, 550 m a.s.l.) (Fig. 1-2-28). Data from Shiga cypress indicated that the highest correlation with mean monthly relative humidity occurred in June at Kyoto meteorological station (r = –0.72, p < 0.001; Fig. 1-2-29a). Significant correlation was also found between tree-ring cellulose δ^{18}O from Nara cedar and June relative humidity (r = –0.70, p < 0.001; Fig. 1-2-29b). However, as of now, there are no tree-ring cellulose δ^{18}O data over the past millennium.

インターネット公表に関する同意が
得られなかったため非公表

Fig 1-2-25. Tree-ring sites of Southeast Asia (Xu et al., 2013). Northern Laos site is Phu Leuy (PL) mountain area (19.9°N, 101.2°E; Xu et al., 2013), and northern Vietnam site is Mu Cang Chai (MCC) area (21°40'N, 104°06'E; Sano et al., 2012).

インターネット公表に関する同意が

得られなかったため非公表

Fig 1-2-26. (a) Comparison of two tree-ring $\delta^{18}O$ chronologies from Southeast Asia (Xu et al., 2013). Red and blue solid lines indicate tree-ring cellulose $\delta^{18}O$ from northern Laos (Xu et al., 2013) and northern Vietnam (Sano et al., 2012), respectively. (b) 31-year running correlation between Laos and Vietnam tree-ring cellulose $\delta^{18}O$ (Sano et al., 2012; Xu et al., 2013).

Fig. 1-2-27. Comparisons of tree-ring cellulose $\delta^{18}O$ from (a) *Q. crispula* and (b) *A. sachalinensis* (Nakatsuka et al., 2004). (c) and (d) also show the similar comparisons, except for the tree-ring cellulose $\delta^{13}C$.

インターネット公表に関する同意が
得られなかったため非公表

Fig. 1-2-28. Map showing tree-ring sites in central Japan (Yamaguchi et al., 2012). Squares indicate tree-ring sites, and circles represent meteorological stations.

インターネット公表に関する同意が
得られなかったため非公表

Fig. 1-2-29. (a) Comparison with Shiga cypress δ^{18}O (black symbols and dashed line) and monthly averaged relative humidity in June at Kyoto meteorological station (green line) (Yamaguchi et al., 2012). (b) Comparison with Nara cedar δ^{18}O (black symbols and dashed line) and monthly averaged relative humidity in June at Ueno meteorological station (green line) (Yamaguchi et al., 2012).

Previous studies proposed that tree-ring cellulose $\delta^{18}O$ allow reconstructions of low-frequency climate variations without statistical detrending (McCarroll and Loader, 2004). Young et al. (2011) revealed that tree-ring cellulose $\delta^{18}O$ chronology from *Pinus sylvestris* in Norway had no age-related trends (Fig. 1-2-30). They showed that regression line for $\delta^{18}O$ was –0.0001 ‰ per year, indicating that this would lead 0.03‰ differences over the past three centuries. Considering that measurement error was less than 0.3‰, this age-related trend was small.

In contrast, hydrological reconstruction using *Pinus uncinata* in Spanish Pyrenees was confirmed to have age-related low-frequency variation (Fig. 1-2-31; Esper et al., 2010). This non-climatic variation was also exhibited in tree-ring cellulose $\delta^{18}O$ from older and younger tree in central Asia (Treydte et al., 2006). In central Japan, hydroclimate reconstruction using cypress can be impacted by this age-related trend (Nakatsuka, personal communication).

インターネット公表に関する同意が

得られなかったため非公表

Fig. 1-2-30. Individual 28 tree-ring cellulose $\delta^{18}O$ chronologies from *Pinus sylvestris* in Norway (Young et al., 2011). Black solid line indicates the regression line for $\delta^{18}O$.

インターネット公表に関する同意が

得られなかったため非公表

Fig. 1-2-31. Age-related trends for $\delta^{18}O$, $\delta^{13}C$, maximum latewood density (MXD) and tree ring width (TRW) (Esper et al., 2010).

1-2-6. Relationship between the East Asian Summer Monsoon and El Niño–Southern Oscillation

On annual and inter-annual time scales, different mechanisms can influence the East Asian climate variability. Previous work identified the El Niño–Southern Oscillation (ENSO) had a potentially important controlling factor for the EASM in these time scales (e.g., Wang et al., 2000; Wu and Wang, 2002). Given the short duration of the instrumental temperature and precipitation records, proxy-based environmental reconstructions are needed to better understand the longer-term changes in inter-annual relationship of the ENSO-EASM teleconnection. Several studies reconstructed ENSO history throughout the Holocene (e.g., Cobb et al., 2003, 2013; McGregor and Gagan., 2004; McGregor et al., 2013; Li et al., 2011, 2013). However, at present, there are few studies that have reconstructed hydrological variability at annual resolution in East Asia including Japan (Fig. 1-2-17). Annually resolved hydroclimate reconstructions allow for considerations of the inter-annual relationship between the ENSO and hydrological conditions in Japan.

1-2-7. Research objectives and thesis structure

As mentioned in this chapter, long-term hydrological conditions in East Asia indicate complicated rainfall pattern during the last millennium. A previous study proposed that the El Niño-like and La Niña-like equatorial Pacific conditions play an important role in East China (Chen et al., 2015). However, there are not enough proxy records in eastern China and its surroundings to discuss about the rainfall pattern (Chen et al., 2015). Hydrological reconstructions in central Japan may shed light on this issue, because the EOF analysis based on the annual precipitation indicates the clear decrease during the modern period (AD 1900–2008) (Fig. 1-2-16). Rainfall pattern analysis for the modern period (AD 1900–2008) also indicated that this proposal was not able to explain for the long-term precipitation increase in Nansei Islands including Yakushima Island. Hydroclimate reconstruction in Yakushima Island may develop understanding about another mechanism for long-term rainfall pattern in eastern part of East Asia. To understand long-term precipitation trends regarding these issues, hydrological reconstructions are needed in central Japan and Yakushima Island. In addition, different mechanisms can influence on the East Asian climate variability on annual and inter-annual time scales. ENSO had a potentially important controlling factor for the EASM in these time scales, and proxy-based environmental reconstructions are needed to better understand the longer-term changes in inter-annual relationship of the ENSO-EASM teleconnection. However, there are still no studies that have reconstructed annually resolved hydrological variations in Japan over the past millennium.

To reconstruct long-term hydrological conditions in Japan, I focused on tree-ring cellulose $\delta^{18}O$ using Japanese cedars. This is because a previous study proposed that tree-ring cellulose $\delta^{18}O$ using tree of redwood family (*Sequoia sempervirens*) allowed reconstructions of both high- and low-frequency hydrological variations (Johnstone et al., 2013). Thus, I focused on cedar trees (redwood family) to reconstruct long-term hydrological conditions in Japan.

Previous studies reported that low-frequency hydrological variations reconstructed using this proxy can be impacted by age-related trend (e.g., Treydte et al., 2006; Esper et al., 2010). Thus, age trend test is needed to consider that cedar trees are

suitable to reconstruct long-term hydrological conditions.

Generally, this climate proxy is validated by comparisons with meteorological datasets. The highest correlation indicates main factor of tree-ring cellulose $\delta^{18}O$ changes (e.g., Yamaguchi et al., 2010; Li et al., 2015). These analyses also suggest the main growth period. Previous studies reported that tree-ring cellulose $\delta^{18}O$ from Japanese cedar has the highest correlation with June relative humidity (e.g., Yamaguchi et al., 2010). However, these reconstructions were based on empirical relations between tree-ring cellulose $\delta^{18}O$ and meteorological data. Thus, this proxy was without confidence that cedar trees mainly grow during the early summer period. To increase a reliability of tree-ring cellulose $\delta^{18}O$, tree-ring growth rate measurements are necessary at tree-ring sites. In this thesis, I observed tree-ring growth rates in Yakushima Island.

The main objective of this study is reconstructing annual hydrological changes in Japan. To reconstruct long-term hydrological condition, I used tree-ring cellulose $\delta^{18}O$ from cedar trees in Japan. In chapter 2, two long cedar tree-ring $\delta^{18}O$ chronologies from central Japan are presented over the past 400 years. These datasets allow me consider that Japanese cedars are able to reconstruct the low-frequency hydroclimate. In chapter 3, I report another tree-ring cellulose $\delta^{18}O$ chronology in Yakushima Island from the MCA and LIA. In this site, my observations of tree-ring growth rates and meteorological data allow me to confirm a reliability of reconstructions using tree-ring cellulose $\delta^{18}O$. Based on these datasets, I discussed about possible influences of the Pacific SST on the long-term hydrological variations in central Japan (Chapter 4) and Yakushima Island (Chapter 5). In Chapter 6, inter-annual relationship between ENSO and tree-ring cellulose $\delta^{18}O$ was investigated. In the last chapter, I provide general discussion and future perspectives of this thesis (Chapter 7). This discussion can develop understanding about the mechanism for long-term rainfall pattern in eastern part of East Asia and inter-annual relationship between ENSO-EASM teleconnection.

# Chapter 2

Tree-ring cellulose oxygen isotopes in central Japan

2-1. Chapter objective

In this chapter, I present two tree-ring $\delta^{18}O$ chronologies in central Japan using Japanese cedars over the past four centuries. In central Japan, Yamaguchi et al. (2010) presented a cedar tree-ring cellulose $\delta^{18}O$ series from AD 1612 to 1756. Here I additionally report tree-ring cellulose $\delta^{18}O$ results that extend the continuous portion of this central Japanese record from AD 1757 to 1935. To examine a reliability of long-term hydroclimate reconstruction using this proxy, I also present a new cedar tree-ring cellulose $\delta^{18}O$ chronology in central Japan from AD 1600 to 1959. Comparison and statistical analysis allow me to test whether low-frequency hydroclimate reconstructions using Japanese cedar tree-ring cellulose $\delta^{18}O$ are necessary to remove nonclimatic age related trends.

2-2. Materials and Methods

2-2-1. Samples

I measured tree-ring cellulose $\delta^{18}O$ on two samples from central Japan. A Japanese cedar (*Cryptomeria japonica*) was collected by Dr. Masao Ohuchi (Kyoto University) at Ise grand shrine in Mie prefecture (34°27′N, 136°44′E; Fig. 2-2-1) during Ise Bay typhoon (AD 1959). This tree grew from AD 1501 to 1959. I also measured cellulose $\delta^{18}O$ on the same Japanese cedar (*Cryptomeria japonica*) as Yamaguchi et al. (2010), which was acquired from Muroji temple in Nara prefecture (34°32'N, 136°02'E, 405 m a.s.l.; Fig. 2-2-2). This old tree grew from AD 1607 to 1998.
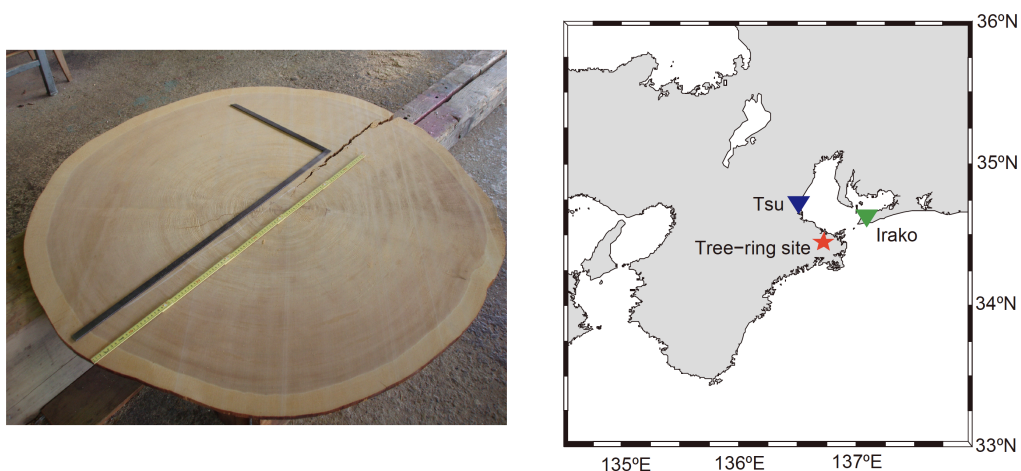
Fig. 2-2-1. Japanese cedar collected at Ise grand shrine in Mie prefecture (left). Map showing sampling site and meteorological stations (right). Red star indicates tree-ring site, and downward triangles indicate meteorological stations.
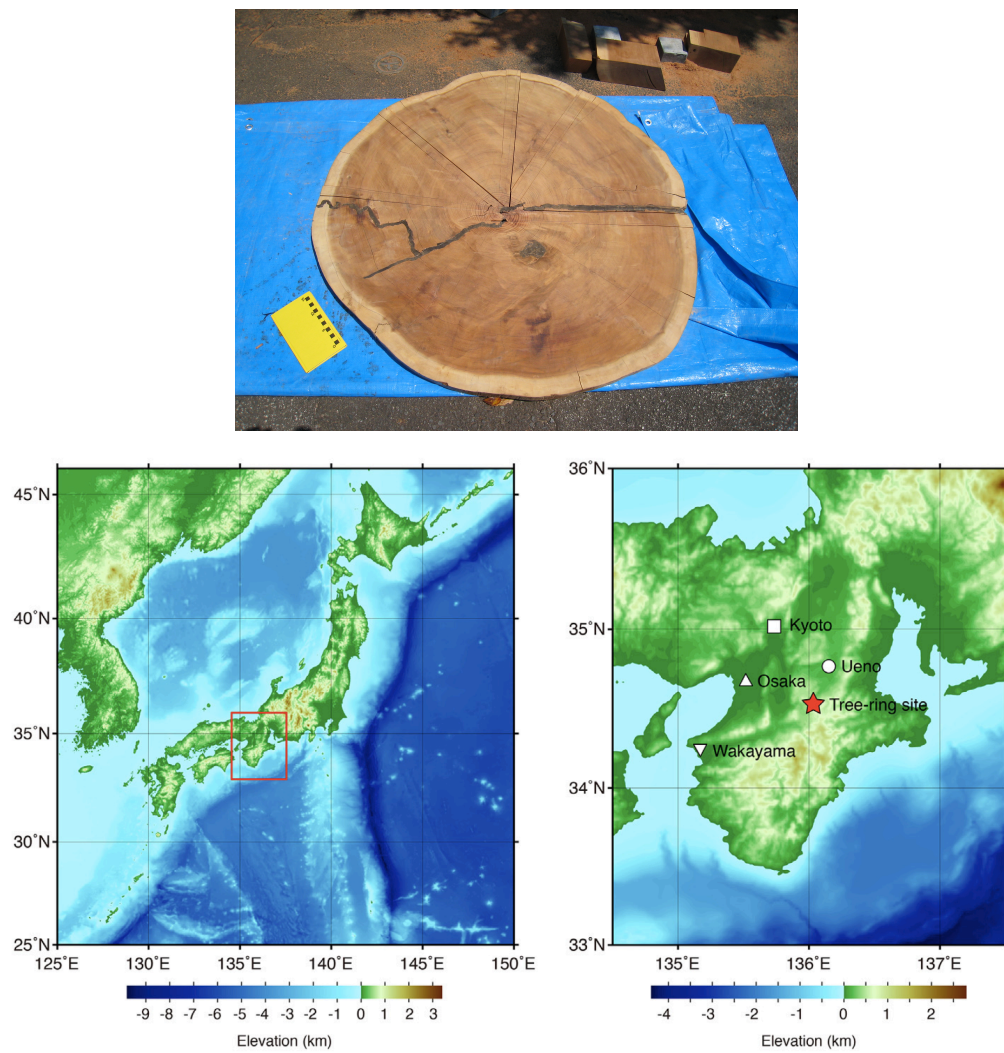
Fig. 2-2-2. Japanese cedar acquired from Muroji temple in Nara prefecture (top). Map showing tree-ring site and meteorological stations (bottom). Symbols indicate tree-ring site (red star), Osaka (upward triangle), Kyoto (square), Wakayama (downward triangle) and Ueno (circle) meteorological stations.

2-2-2. Age determinations

I determined Mie cedar age using dendrodaiting. Dendrochronology is a standard technique to decide tree-ring sample age. Tree-ring width pattern of Mie cedar is shown in Fig. 2-2-3. Comparison between this variation and standard pattern in central Japan was able to determine this tree-ring sample age.

Nara cedar was previously dated by Miyahara et al. (2004) via a combination of dendrodating and identification of the AD 1964 Δ^{14}C "Bomb peak". Based on these age determinations, I measured tree-ring cellulose δ^{18}O in central Japan.

2-2-3. Measurement of tree-ring cellulose δ^{18}O

To extract α-cellulose from my tree-ring samples, I applied "plate method" (Xu et al., 2011) to obtain cellulose plates from sliced wood samples (Fig. 2-2-4). First, I cut tree-ring sample into plates using a low speed diamond wheel saw (thickness: 1 mm). To remove lipids, these plates were treated with toluene and ethanol (1:1) in an ultrasonic water bath for 30 min. Similar step with acetone had been repeated. After lipid removes, these samples were treated with acidified $NaClO_2$ in a water bath (70 ℃) for 60 min to decompose lignin. This step was repeated four times. To remove hemicellulose, I poured a 17wt% NaOH solution into tubes containing wood samples. These tubes were in a water bath (80 ℃) for 45 min, and this treatment repeated three times. After this treatment, these were washed with a diluted HCl solution. These extracted cellulose plates were then divided up into individual annual growth rings, and these separated samples (0.2 mg) were wrapped in silver foil for duplicate measurements of tree-ring cellulose δ^{18}O.
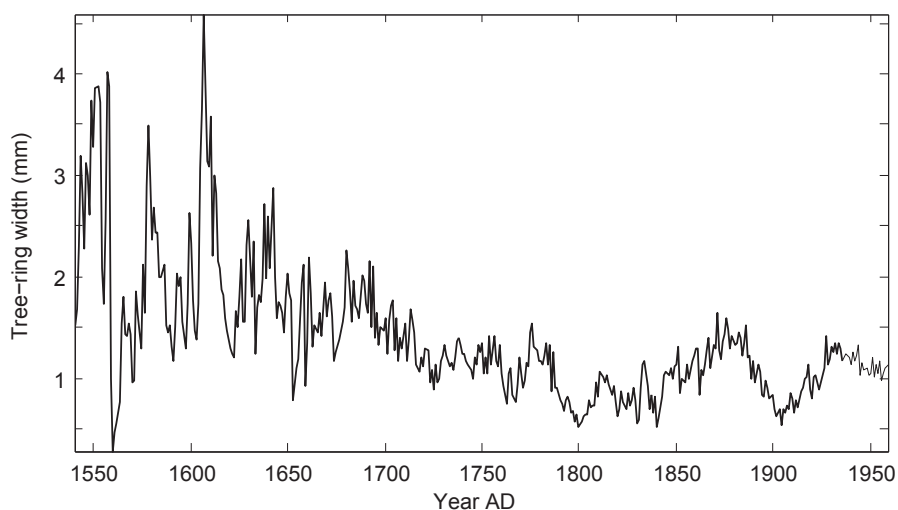
Fig. 2-2-3. Mie cedar tree-ring width pattern. Black solid line indicates mean of duplicate measurements.
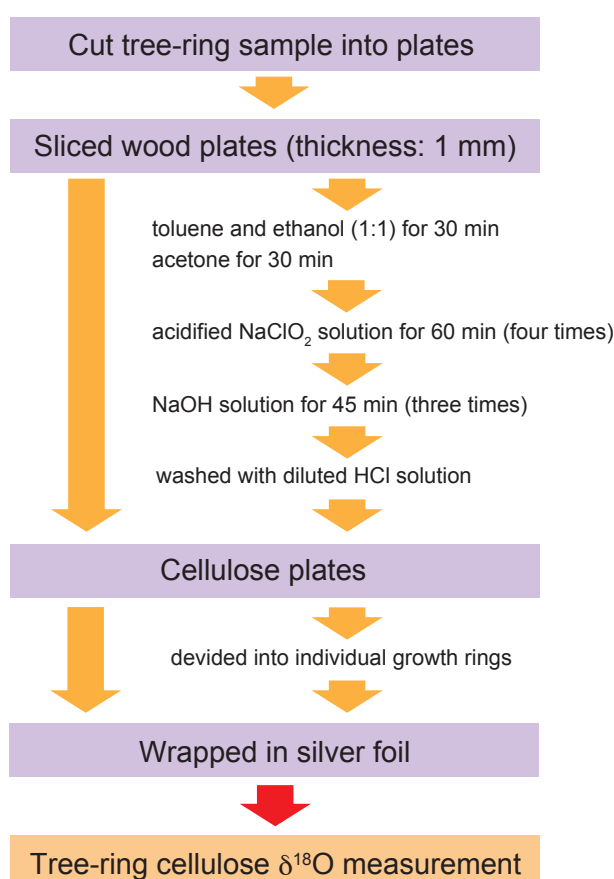
Fig. 2-2-4. Schematic diagram of sample preparation.

To measure tree-ring cellulose $\delta^{18}O$, I used a continuous flow high temperature thermal conversion elemental analyzer (TCEA) and a Thermo Finnigan MAT253 mass spectrometer (Fig. 2-2-5 and Fig. 2-2-6) at Tokyo Institute of Technology for the analyses. α-cellulose was converted to CO gas at 1450 ℃.

$$C_6H_{10}O_5 \rightarrow 5CO + 10H_2 + C$$

In isotope ratios measurements, the measured values generally indicate the difference between sample and reference gas δ values (e.g., Sato and Suzuki, 2010). This is because reference gas had little inhomogeneous property. In my measurement, reference CO gas was measured with cellulose. Here, the reference gas $\delta^{18}O$ was defined as 0‰. Thus, the measurement oxygen isotope values indicate the difference between cellulose and reference gas $\delta^{18}O$. To confirm the measurement reliability, I duplicated the reference gas measurements (Fig. 2-2-7).

This TCEA machine was introduced into Tokyo Institute of Technology in 2012 and was set up for oxygen isotope measurement. Two particular areas of the instrument were upgraded. Firstly, the auto-sampler was improved to measure more than 90 samples. The one disc default setup for this machine is able to measure 31 tree-ring cellulose samples (Fig. 2-2-8a). The original setup was not able to saturate multi-disc with helium gas. To overcome this problem, I set up a closed container around the auto-sampler (Fig. 2-2-8b). To smoothly introduce wrapped cellulose sample into TCEA, the sample chamber was also improved (Fig. 2-2-8c). To decide the most suitable mass for each measurement, I measured tree-ring cellulose $\delta^{18}O$ for various working standard mass (Merck cellulose) (Fig. 2-2-9). Results for less than 200 μg indicated relatively heavy oxygen isotopes. Thus, I determined the necessary mass required for cellulose measurement to be over 200 μg. To examine the calibration line, I measured tree-ring cellulose $\delta^{18}O$ for two standard cellulose samples (Merck cellulose and IAEA-C3) (Table 2-2-1). The mean difference between Merck cellulose and reference gas $\delta^{18}O$ showed 15.12±0.13‰, and that of IAEA-C3 was 20.30±0.15‰. The difference of these values is about 5.2‰. To compare my tree-ring cellulose $\delta^{18}O$ measurement values with other oxygen isotope data from different laboratories, oxygen

isotope data are generally expressed as follows: $\delta^{18}O = (({}^{18}O/{}^{16}O)_{sample}/({}^{18}O/{}^{16}O)_{standard} - 1)$ × 1000 (‰), where the standard used was Vienna Standard Mean Ocean Water (VSMOW). Here, recommended cellulose oxygen isotope ratios indicate the difference of VSMOW. Recommended Merck cellulose value is 27.5‰ (VSMOW), and that of IAEA-C3 is 32.7‰ (VSMOW), indicating that the difference of these recommended values is 5.2‰. This is the same value as my two standard cellulose measurements. Based on these measurements, I determined the calibration line.

In tree-ring samples from central Japan, measurement uncertainties were less than 0.3‰ according to the standard deviation calculated from repeated analyses of a working standard (Merck cellulose). Hereafter, the data were expressed as oxygen isotope ratios as follows: $\delta^{18}O = (({}^{18}O/{}^{16}O)_{sample}/({}^{18}O/{}^{16}O)_{standard} - 1)$ × 1000 (‰), where the standard used was VSMOW.
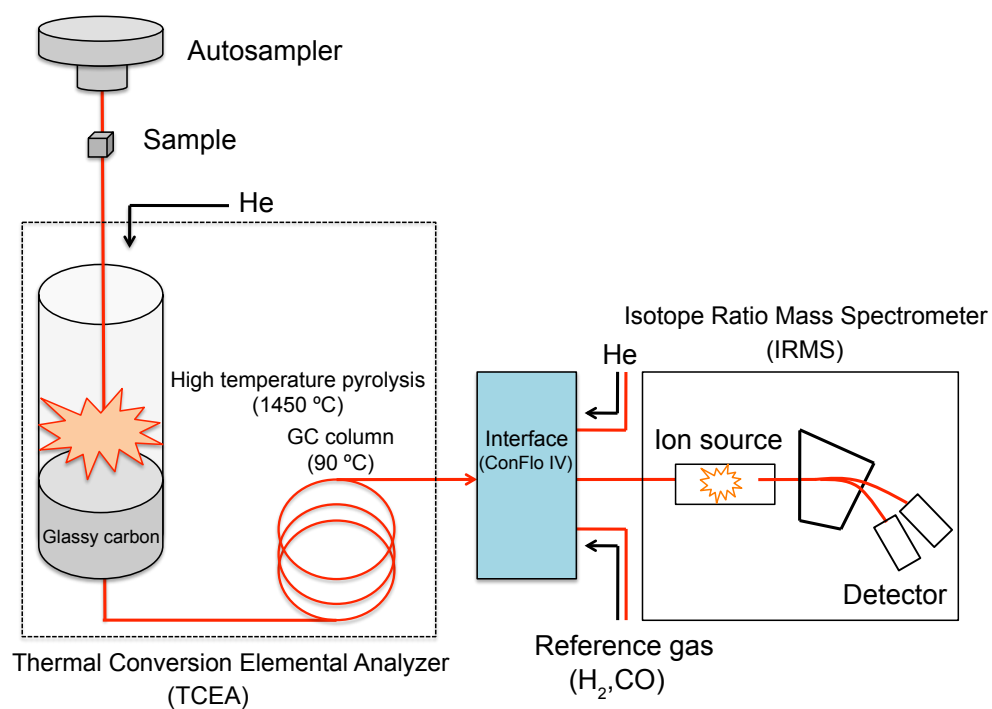
Fig. 2-2-5. Schematic diagram of TCEA (modified from Suzuki and Sato, 2010).
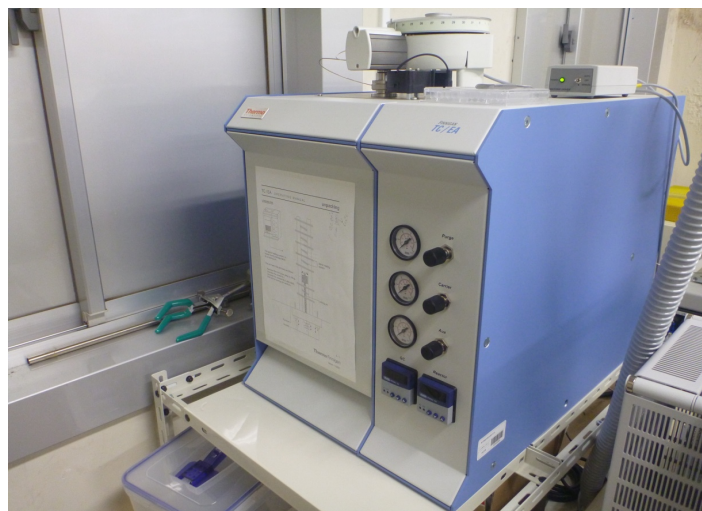
Fig. 2-2-6. TCEA machine at Tokyo Institute of Technology.
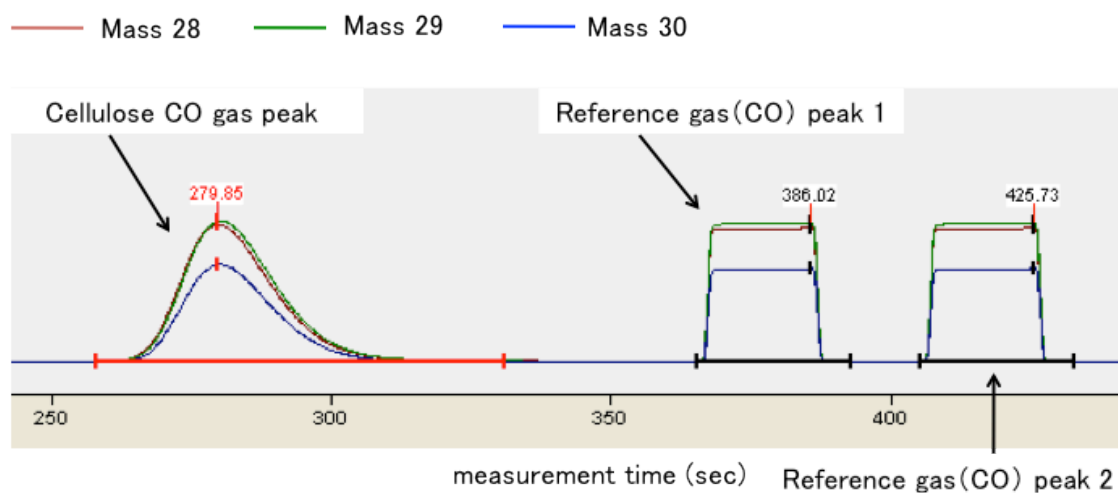
Fig. 2-2-7. TCEA measurement sequence. Brown, green and blue lines indicate mass 28 ($^{12}C^{16}O$), 29 ($^{13}C^{16}O$) and 30 ($^{12}C^{18}O$), respectively. Spectrum amplitudes indicate the mass intensity (mV).

55
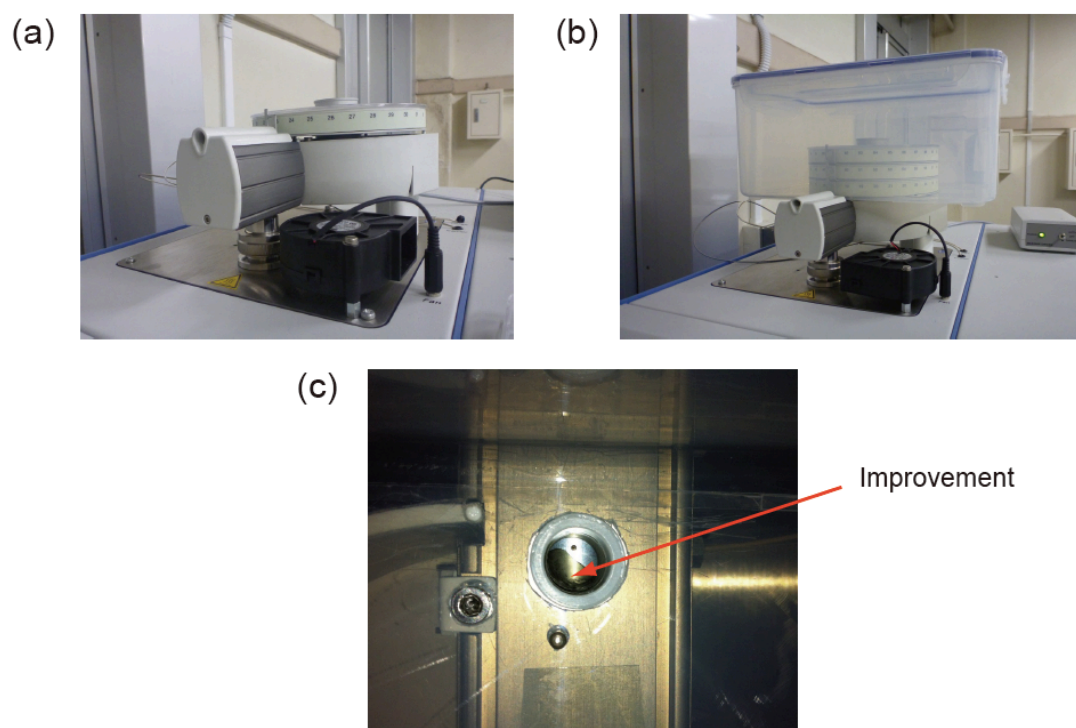
Fig. 2-2-8. (a) Beginning condition of auto-sampler, and (b) after improvement. (c) Improved inner part of this machine.
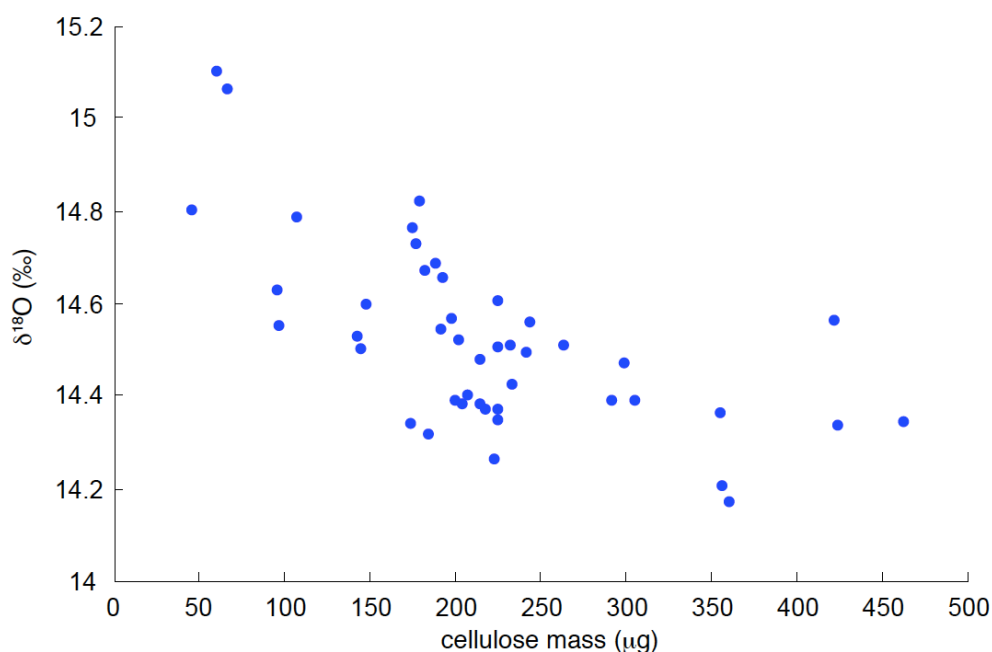
Fig 2-2-9. Tree-ring cellulose $\delta^{18}O$ for various mass of working standard (Merck cellulose). Here measurement oxygen isotope values indicate the difference between cellulose and reference gas $\delta^{18}O$.

	IAEA-C3	Merck
Measurement 1	20.28‰	15.27‰
Measurement 2	20.45‰	15.18‰
Measurement 3	20.10‰	15.05‰
Measurement 4	20.37‰	14.98‰
Average	20.30±0.15‰	15.12±0.13‰

Table 2-2-1. Results of tree-ring cellulose $\delta^{18}O$ for two standard cellulose samples (Merck cellulose and IAEA-C3). Here measurement oxygen isotope values indicate the difference between cellulose and reference gas $\delta^{18}O$.

2.3. Results and Discussion

2-3-1. Comparison with meteorological data

インターネット公表に関する共著者全員の
同意が得られていないため、
本章の一部については、非公開

インターネット公表に関する共著者全員の
同意が得られていないため、
本章の一部については、非公開

インターネット公表に関する共著者全員の
同意が得られていないため、
本章の一部については、非公開

Fig. 2-3-1.

インターネット公表に関する共著者全員の
同意が得られていないため、
本章の一部については、非公開

Fig. 2-3-2.

インターネット公表に関する共著者全員の
同意が得られていないため、
本章の一部については、非公開

Fig. 2-3-3.

インターネット公表に関する共著者全員の
同意が得られていないため、
本章の一部については、非公開

Fig. 2-3-4.

2-3-2. Validations for tree-ring cellulose δ^{18}O in central Japan

インターネット公表に関する共著者全員の

同意が得られていないため、

本章の一部については、非公開

インターネット公表に関する共著者全員の
同意が得られていないため、
本章の一部については、非公開

インターネット公表に関する共著者全員の
同意が得られていないため、
本章の一部については、非公開

インターネット公表に関する共著者全員の
同意が得られていないため、
本章の一部については、非公開

Fig. 2-3-5.

インターネット公表に関する共著者全員の
同意が得られていないため、
本章の一部については、非公開

Fig. 2-3-6.

インターネット公表に関する共著者全員の
同意が得られていないため、
本章の一部については、非公開

Fig. 2-3-7.

インターネット公表に関する共著者全員の

同意が得られていないため、

本章の一部については、非公開

Fig. 2-3-8.

インターネット公表に関する共著者全員の
同意が得られていないため、
本章の一部については、非公開

Fig. 2-3-9.

インターネット公表に関する共著者全員の
同意が得られていないため、
本章の一部については、非公開

Fig. 2-3-10.

インターネット公表に関する共著者全員の
同意が得られていないため、
本章の一部については、非公開

Table 2-3-1. Negative and positive value years for Mie tree-ring cellulose $\delta^{18}O$ chronology during the LIA (AD 1681–1850).

インターネット公表に関する共著者全員の
同意が得られていないため、
本章の一部については、非公開

Table 2-3-2. Negative and positive value years for Nara tree-ring cellulose $\delta^{18}O$ chronology during the LIA (AD 1681–1850).

インターネット公表に関する共著者全員の
同意が得られていないため、
本章の一部については、非公開

Table 2-3-3. Negative and positive value years for Mie tree-ring cellulose $\delta^{18}O$ chronology during AD 1900–1959.

インターネット公表に関する共著者全員の
同意が得られていないため、
本章の一部については、非公開

Table 2-3-4. Negative and positive value years for Nara tree-ring cellulose $\delta^{18}O$ chronology during AD 1900–1935.

2.4. Summary

インターネット公表に関する共著者全員の
同意が得られていないため、
本章の一部については、非公開

Chapter 3

Tree-ring cellulose oxygen isotopes in Yakushima Island

3-1. Chapter objective

Generally, tree-ring cellulose δ^{18}O is validated by comparisons with meteorological datasets. The highest correlation indicates main factor of tree-ring cellulose δ^{18}O changes (e.g., Yamaguchi et al., 2010; Li et al., 2015). These analyses also suggest the main growth period. However, these reconstructions were based on empirical relations between tree-ring cellulose δ^{18}O and meteorological data. Thus, this proxy was without confidence that cedar trees mainly grow during the early summer period. To increase a reliability of tree-ring cellulose δ^{18}O, tree-ring growth rate measurements are necessary at tree-ring sites.

In this chapter, I measured stem-growth rates at tree-ring site in Yakushima Island. These measurements allow me to confirm a reliability of reconstructions using tree-ring cellulose δ^{18}O. Based on these observations and validations, I present a tree-ring cellulose δ^{18}O chronology in Yakushima Island from the MCA and LIA.

3-2. Materials and Methods

3-2-1. Samples

Here I measured tree-ring cellulose δ^{18}O on a disc of Yakusugi (*Cryptomeria japonica*), which was collected at Ishizuka area in Yakushima Island (30°20′ 178'N, 130°32′ 50'E, 900 m a.s.l.; Fig 3-2-1) in AD 1956. This cedar grew from AD 62 to 1956. This tree-ring sample overlap with meteorological data only for AD 1938 to 1956, and tree ring widths became too narrow to continuously separate individual growth rings after AD 1805. Thus, I also measured another Japanese cedar core in Ishizuka area during the recent period.
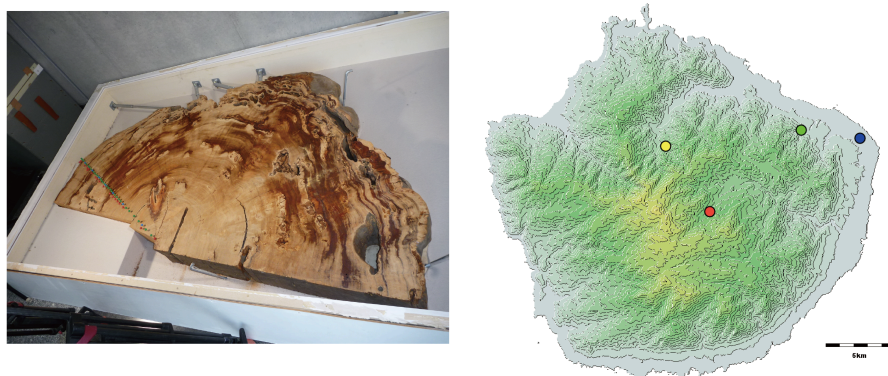
Fig. 3-2-1. Japanese cedar acquired from Yakushima in Kagoshima prefecture (left panel). Map showing sampling site and meteorological station (right panel). Symbols indicate Ishizuka (red circle), Tabugawa (green circle) and Yakushima weather station (blue circle).

3-2-2. Age determinations

This 1895-year tree sample was dated by three methods. In the early part of Yakushima cedar from AD 173 to 743, I determined the age by dendrodating (tree-ring width pattern matching). Based on this age determination, radiocarbon measurements were performed around late 8th century using Accelerator Mass Spectrometry (AMS) at Yamagata University. A previous study identified a rapid radiocarbon (^{14}C) content increase from AD 774 to 775 (Miyake et al., 2012). Temporal percent modern carbon variation indicates the same rapid increase (Fig. 3-2-2), and this ^{14}C peak identification enables us to determine the age of this tree-ring chronology. After the late 8th century, we counted the annual rings of this sample. To correctly count, I also confirmed the individual rings under a binocular microscope (Fig. 3-2-3).

インターネット公表に関する共著者全員の
同意が得られていないため、
本章の一部については、非公開

Fig. 3-2-2. Temporal percent modern carbon variation around late 8th century from Yakushima tree-ring sample.
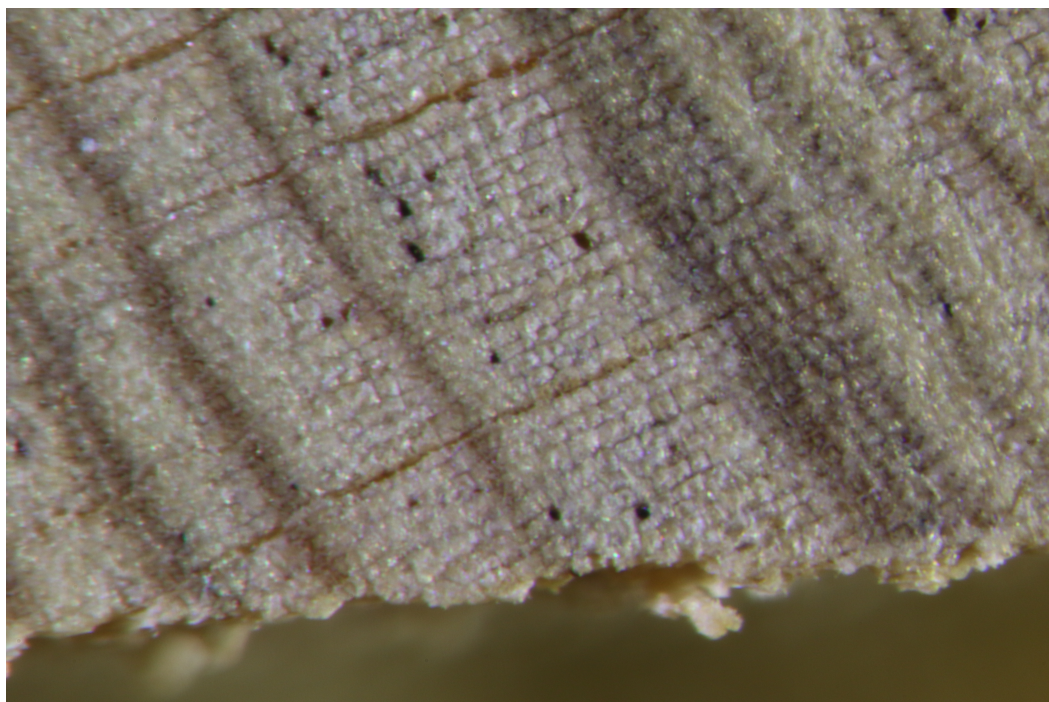
Fig 3-2-3. An example of magnified photo for Yakushima cedar.

3-2-3. Measurement of tree-ring cellulose $\delta^{18}O$

To extract α-cellulose from a disc sample, I applied Jayme and Wise method (e.g., Loader et al., 1997; Loader et al., 2003). First, I cut this tree-ring sample into plates using a diamond wheel saw (thickness: 0.5–1 mm). These plates were then divided up into individual annual growth rings. α-cellulose was extracted from these divided samples based on the same chemical protocol in Chapter 2. These samples were wrapped in silver capsule for duplicate tree-ring cellulose $\delta^{18}O$ measurements. In a core sample, I applied same method in Chapter 2.

In this measurement, I also used a TC/EA and a Thermo Finnigan MAT253 mass spectrometer at Tokyo Institute of Technology (additional details can be found in Chapter 2). The measurement uncertainties were less than 0.3‰ according to the standard deviation calculated from repeated analyses of a working standard (Merck cellulose).

3-2-4. Meteorology and stem growth rates in Yakushima Island

Observations

I observed tree-ring growth rates of 50 cedars (Fig. 3-2-4a), including 20 trees in Ishizuka and 30 trees in Tabugawa (30°23′ 47'N, 130°30′ 52'E, 180 m a.s.l.; Fig 3-2-1) areas. In this observation, I used dendro-meters to measure stem growth rates. This accuracy of tree-ring diameter measurement was within 1 mm.

To investigate meteorological conditions in tree-ring site, I also observed temperature and relative humidity (Fig. 3-2-4b). Here I used Thermo-hydrometers (temperature accuracy ±0.2 °C at 0–50 °C and humidity accuracy ±2.5% relative humidity at 10–90 °C). This equipment was set up to monitor meteorological variations at Ishizuka area (Fig 3-2-1).

Fig. 3-2-4. (a) Measurements of stem growth rates. (b) Meteorological observations at Ishizuka area. (c) 1895-year cedar sample at Ishizuka.

Tree-ring stem growth rate in Yakushima

Observation indicated that main tree-ring growth interval was from May to June at Ishizuka area. Average radial stem growth rates showed that 60% annual growth occurred at May–June (MJ) period (Fig. 3-2-5d and Fig. 3-2-6). This stem growth variation was similar to that of Tabugawa area, but the annual growth at Tabugawa area gradually increased. I could find that about 30% annual growth occurred at the same period (MJ) (Fig. 3-2-5c and Fig. 3-2-7).

Meteorological condition in the tree-ring site

Observation showed that temporal temperature variation at Ishizuka area was similar to that of Yakushima weather station, but the amplitude was different (Fig 3-2-5ab). This observation also indicated that relative humidity at Ishizuka area was mainly more than 95% from June (Fig 3-2-8). Relative humidity comparison indicated that temporal ralative humidity variation at tree-ring site was different from that of Yakushima station (Fig 3-2-8). These may relate to altitude difference between tree-ring site (Ishizuka) and Yakushima station.

インターネット公表に関する共著者全員の
同意が得られていないため、
本章の一部については、非公開

Fig. 3-2-5. Comparisons of daily mean temperature (top) and average radial stem growth rates (bottom) in Yakushima Island.

インターネット公表に関する共著者全員の

同意が得られていないため、

本章の一部については、非公開

Fig. 3-2-6. Monthly tree-ring growth rate at Ishizuka area.

インターネット公表に関する共著者全員の

同意が得られていないため、

本章の一部については、非公開

Fig. 3-2-7. Monthly tree-ring growth rate at Tabugawa area.

インターネット公表に関する共著者全員の
同意が得られていないため、
本章の一部については、非公開

Fig. 3-2-8. Comparison of relative humidity in Yakushima. Circle and square symbols indicate the relative humidity variations at Ishizuka and Yakushima weather station, respectively.

3-3. Results and discussion

3-3-1. Comparison with meteorological data

インターネット公表に関する共著者全員の
同意が得られていないため、
本章の一部については、非公開

インターネット公表に関する共著者全員の
同意が得られていないため、
本章の一部については、非公開

インターネット公表に関する共著者全員の
同意が得られていないため、
本章の一部については、非公開

Fig. 3-3-1.

インターネット公表に関する共著者全員の
同意が得られていないため、
本章の一部については、非公開

Fig. 3-3-2.

インターネット公表に関する共著者全員の
同意が得られていないため、
本章の一部については、非公開

Fig. 3-3-3.

インターネット公表に関する共著者全員の
同意が得られていないため、
本章の一部については、非公開

インターネット公表に関する共著者全員の
同意が得られていないため、
本章の一部については、非公開

Fig. 3-3-4.

インターネット公表に関する共著者全員の
同意が得られていないため、
本章の一部については、非公開

Fig. 3-3-5.

3-3-2. Tree-ring cellulose $\delta^{18}O$ in Yakushima Island over the past millennium

インターネット公表に関する共著者全員の
同意が得られていないため、
本章の一部については、非公開

インターネット公表に関する共著者全員の
同意が得られていないため、
本章の一部については、非公開

Fig. 3-3-6

インターネット公表に関する共著者全員の

同意が得られていないため、

本章の一部については、非公開

Table 3-3-1. Negative and positive value years for Yakushima tree-ring cellulose $\delta^{18}O$ chronology during the MCA (AD 1025–1250).

インターネット公表に関する共著者全員の
同意が得られていないため、
本章の一部については、非公開

Table 3-3-2. Negative and positive value years for Yakushima tree-ring cellulose $\delta^{18}O$ chronology during the LIA (AD 1450–1805).

3-4. Summary

インターネット公表に関する共著者全員の
同意が得られていないため、
本章の一部については、非公開

Chapter 4

Relative humidity reconstruction in central Japan during the Little Ice Age

4-1. Chapter objective

インターネット公表に関する共著者全員の

同意が得られていないため、

本章については、非公開

4-2. Method and data

インターネット公表に関する共著者全員の

同意が得られていないため、

本章については、非公開

4-3. Results and Discussion

4-3-1. Comparison with temperature

インターネット公表に関する共著者全員の
同意が得られていないため、
本章については、非公開

インターネット公表に関する共著者全員の
同意が得られていないため、
本章については、非公開

Fig. 4-1.

4-3-2. Comparison with SST

インターネット公表に関する共著者全員の
同意が得られていないため、
本章については、非公開

インターネット公表に関する共著者全員の
同意が得られていないため、
本章については、非公開

Fig. 4-2.

インターネット公表に関する共著者全員の
同意が得られていないため、
本章については、非公開

Fig. 4-3.

4-4. Summary

インターネット公表に関する共著者全員の

同意が得られていないため、

本章については、非公開

Chapter 5

Hydroclimate reconstruction in Yakushima Island over the past millennium

5-1. Chapter objective

インターネット公表に関する共著者全員の

同意が得られていないため、

本章については、非公開

5-2. Method and data

インターネット公表に関する共著者全員の

同意が得られていないため、

本章については、非公開

5-3. Results and Discussion

5-3-1. Comparison with temperature

インターネット公表に関する共著者全員の
同意が得られていないため、
本章については、非公開

インターネット公表に関する共著者全員の
同意が得られていないため、
本章については、非公開

Fig. 5-1.

5-3-2. Comparison with SST

インターネット公表に関する共著者全員の
同意が得られていないため、
本章については、非公開

インターネット公表に関する共著者全員の
同意が得られていないため、
本章については、非公開

インターネット公表に関する共著者全員の

同意が得られていないため、

本章については、非公開

Fig. 5-2.

インターネット公表に関する同意が
得られなかったため非公表

Fig. 5-3. (top) Map showing the ODP site 1202 in Okinawa Trough (Wu et al., 2012). (bottom) SST reconstruction in Southern Okinawa Trough by analyzing tetraether lipid preserved in the sediment core.

インターネット公表に関する共著者全員の

同意が得られていないため、

本章については、非公開

Fig. 5-4.

インターネット公表に関する同意が

得られなかったため非公表

Fig. 5-5. Differences between 1990s and 1980s for June precipitation (Tomita et al., 2007). Contours are drawn with 30 mm/month interval. Dot-lines are negative anomalies of precipitation. Shading represents the 95% confidence level.

5-4. Summary

インターネット公表に関する共著者全員の
同意が得られていないため、
本章については、非公開

Chapter 6

Relationship between tree-ring cellulose oxygen isotopes in Japan and the El Niño–Southern Oscillation

6-1. Chapter objective

In this chapter, I investigated the relationship between the ENSO and Nara tree-ring cellulose $\delta^{18}O$ over the past ~400 years. My data allowed consideration of long-term changes in the interannual relationship between the ENSO and hydroclimate variability in central Japan.

6-2. Method and data

To examine the relationship between EASM and ENSO, I use a tree-ring cellulose $\delta^{18}O$ chronology from Nara prefecture over the last four centuries (additional details in chapter 2).

I investigate the relationship between the precipitation in central Japan and ENSO during the 20th century using several ENSO indexes to show that results are generally independent of the chosen reconstructions (see appendix of chapter 6). These include the Niño 3.4 index (Trenberth and Stepaniak, 2001), available from the United States National Center for Atmospheric Research http://www.cgd.ucar.edu/cas/catalog/climind/TNI_N34/); a 1894–1984 coral composite that includes records from both the western and eastern edges of the equatorial cold tongue, as well as the Niño 3.4 region (Crowley et al., 2014); a multivariate ENSO index from 1871 (Wolter and Timlin, 2011); a 1301–1992 tree ring ENSO reconstruction (Li et al., 2013); and a 1525–1982 multiproxy ENSO reconstruction (Braganza et al., 2009).

Wavelet analysis (Torrence and Compo, 1998) was used to analyze the relationship between the various ENSO indexes and summer rainfall in central Japan. Specifically, coherency in time-frequency space was determined using wavelet code for Matlab (Grinsted et al., 2004). Multitaper method (MTM) spectral analysis was performed using the software package kSpectra (Ghil et al., 2002) with a significance test based on an AR(1) (red) null hypothesis.

6-3. Results and Discussion

Relationship with ENSO

I compared my tree-ring cellulose $\delta^{18}O$ to the long tree-ring previous November–January (NDJ) ENSO reconstructions of Li et al. (2013). MTM analysis of the ENSO reconstruction over the same interval as my data (1612 to 1935) reveals 4.0-year, 5.2-year, 9.0-year and 10.4-year spectral peaks (Fig. A6-1a). The multiproxy ENSO reconstruction of Braganza (et al., 2009) is highly correlated with the tree-ring ENSO proxy (r = –0.60, p < 0.001, N =324) and exhibits a similar spectrum (Fig. A6-1b).

Comparisons within the time domain indicate that the strength of relationship between inverted tree-ring $\delta^{18}O$ (because tree-ring $\delta^{18}O$ is negatively correlated with hydrological condition) and ENSO varies on multi-decadal timescales (Fig. 6-1a, b). To examine variations in the tree-ring $\delta^{18}O$–ENSO relation, cellulose $\delta^{18}O$ and ENSO reconstructions were normalized to zero mean and unit standard deviation and band-pass filtered (3–8 years). Then correlation coefficients were calculated using a 31-year moving window using both zero and one-year lag (One-year lag is comparing NDJ ENSO reconstruction to the following year's $\delta^{18}O$). This indicates that zero-lag ENSO teleconnections were generally weak throughout most of the interval examined (Fig. 6-1b). Lag-1 correlation was relatively high during the mid-17th, late 18th and late 19th centuries (Fig. 6-1b). Cross-wavelet analysis (Grinsted et al., 2004) for the tree-ring $\delta^{18}O$ and ENSO reconstructions also shows that a common 3–8 year variability only appears during the mid-17th and late 18th centuries (Fig. 6-1c). A similar relationship was noted with the multiproxy ENSO index (Braganza et al., 2009) (Fig. A6-2; See appendix of chapter 6).

Zero-lag ENSO teleconnections can be expected because the changes of western North Pacific (WNP) anomalous anticyclone-warm ocean interaction (Wang et al., 2000). This WNP anticyclone is associated with the slow or rapid decay of canonical ENSO events, which affects the early summer rainfall in East Asia (Yim et al., 2013). However, zero-lag ENSO teleconnections were generally weak throughout the

examined interval, and the one-year lag tree-ring δ^{18}O-ENSO correlation was relatively high during the mid-17th, late 18th and late 19th centuries. Further investigation is needed to clarify relationship between the one-year lag tree-ring δ^{18}O and ENSO.

Li et al. (2013) suggested that ENSO teleconnection were strong (weak) over the pan-Pacific region during intervals of high (low) ENSO variance. This is illustrated by 31-year running, windowed variance calculated for the tree-ring ENSO reconstruction, which exhibits high variance during the mid-17th, late 18th and late 19th centuries (Fig. 6-1d). This corresponds to the times of coherent 3–8 variability in EASM and ENSO activity.
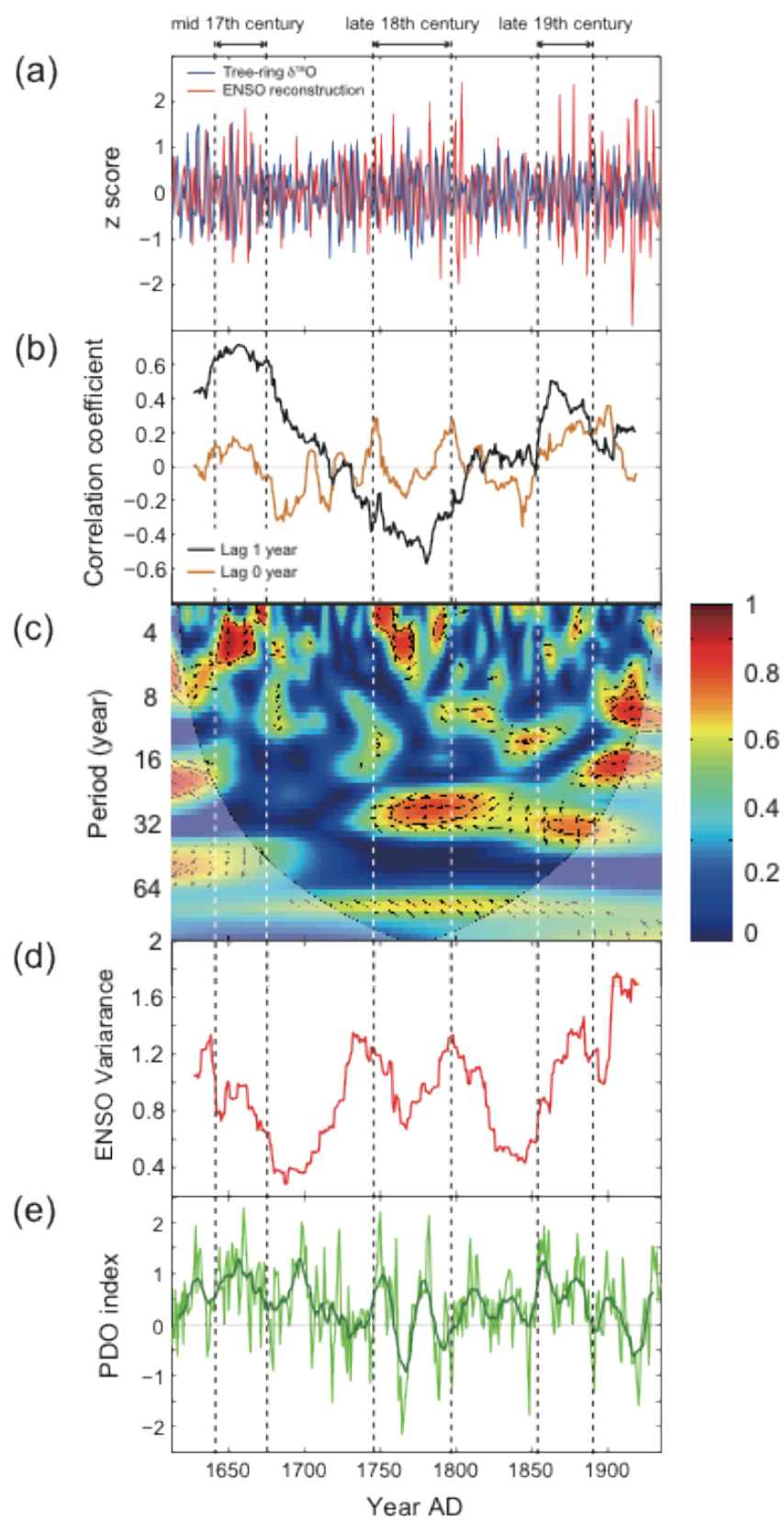
While the correlation between the ENSO reconstruction and inverted tree-ring δ^{18}O is positive during the mid-17th and late 19th centuries, a negative correlation is exhibited during the late 18th century (Fig. 6-1b). This may relate to the Pacific Decadal Oscillation (PDO; Mantua et al., 1997) phase on the relationship between ENSO and EASM (Chan and Zhou, 2005; Yoon and Yeh, 2010; Feng et al., 2014). Reconstructed PDO phases (D'Arrigo and Wilson, 2006) were positive during the mid-17th and late 19th centuries but mainly negative during late-18th century (Fig. 6-1e). It appears that early summer monsoon rainfall may have positive (negative) correlation to ENSO activity when ENSO variance is high during the positive (negative) PDO phases, as previously noted by Yoon and Yeh (2010).

As the tree-ring δ^{18}O chronology is not continuous from 1936 to 1978, I investigated the relationship during the 20th century between the early summer monsoon rainfall over central Japan and several ENSO indexes by using the instrumental Wakayama MJ precipitation. First, I compared the high frequency (3–8 year) Wakayama MJ precipitation with winter (from previous November to January) Niño3.4 index (Trenberth and Stepaniak, 2001) (Fig. 6-2a). (Before the comparison, these datasets were normalized.) 31-year running lag-1 correlation coefficients between the high frequency Wakayama MJ precipitation and the Niño 3.4 index (Trenberth and Stepaniak, 2001) showed that there was little relationship between ENSO and EASM except for late 20th century (Fig. 6-2b). Cross-wavelet analysis also indicates that high-frequency variability appeared from 1980s (Fig. 6-2c). Similar results were obtained with other ENSO indexes (Wolter and Timlin, 2011; Li et al., 2013; Crowley et al., 2014), except for the multiproxy ENSO reconstruction (Braganza et al., 2009),

which only extends to 1982 (See appendix of chapter 6). This is similar to the observation that the relationship between ENSO and EASM strengthened since the late 1970s (e.g., Wang et al., 2008).

To understand the relationship of the ENSO variance and the PDO phase on the relation between EASM and ENSO during the 20th century, I also calculated a 31-year running variance for the Niño 3.4 index (Fig. 6-2d) and instrumental PDO index (Fig. 6-2e). The ENSO variance has been high since 1980 (Fig. 6-2d) while PDO was positive (Fig. 6-2e). Early summer monsoon rainfall during the 20th century is positively correlated with Niño 3.4 when ENSO variance is high during the PDO positive phases.

Previous analyses of the instrumental precipitation records have proposed that the PDO phase can relate to the relationship between the EASM and ENSO during the 20th century (Chan and Zhou, 2005; Yoon and Yeh, 2010; Feng et al., 2014). My annually resolved tree-ring cellulose $\delta^{18}O$ and various comparisons suggest that recent relationship between the PDO phase and the EASM-ENSO teleconnection may be not only a recent phenomenon but also a more persistent feature of the tropical climate system over the past 400 years. To develop this suggestion, we need further annually resolved reconstructions of rainfall spatiotemporal variability over the East Asia.

Fig. 6-1. (a) Comparison of 3–8 year tree-ring $\delta^{18}O$ (inverted) variability with winter ENSO reconstruction (Li et al., 2013). Blue and red solid lines indicate the tree-ring $\delta^{18}O$ and ENSO reconstruction, respectively. (b) 31-year running correlation between the high frequency (3–8 year) tree-ring $\delta^{18}O$ (inverted) and ENSO reconstruction (Li et al., 2013). Orange and black solid lines indicate the correlation coefficients of lag 0-year and lag 1-year, respectively. (c) Wavelet coherence between the tree-ring $\delta^{18}O$ and tree-ring ENSO reconstruction (Li et al., 2013). Black contour means the 95% significant level, and white shade corresponds the cone of influence.Arrows mean the relative phase relation. (d) 31-year running variances for normalizedENSO reconstruction (Li et al., 2013). (e) Reconstruction of the PDO index (D'Arrigo and Wilson, 2006). Green solid line indicates 11 year moving average.
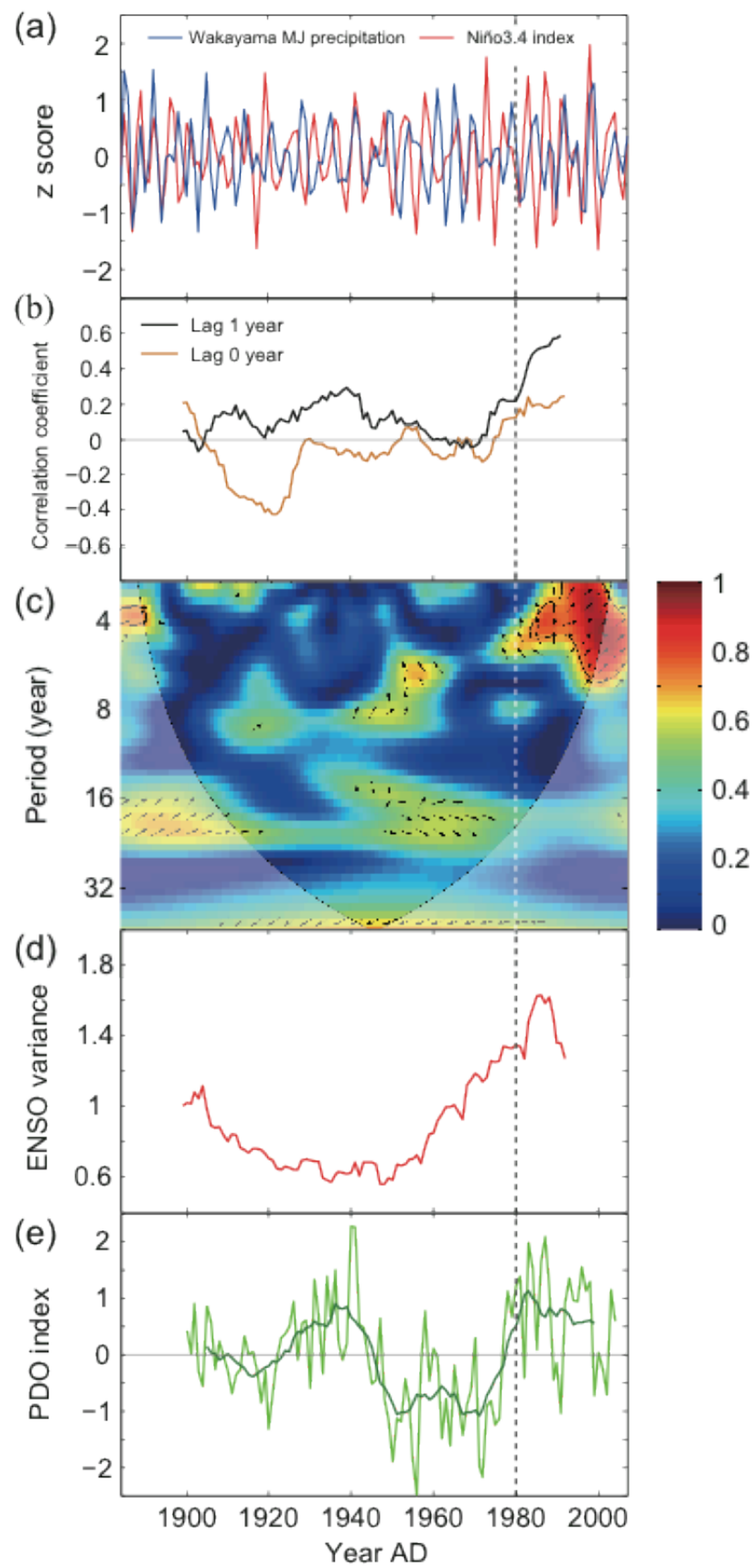
Fig. 6-2. (a) Comparison of high frequency (3–8 year) Wakayama MJ precipitation with winter (previous November–January) Niño 3.4 index (Trenberth and Stepaniak, 2001). Blue and red solid lines indicate the Wakayama MJ precipitation and the Niño 3.4 index, respectively. (b) 31-year running correlation between the high frequency (3–8 year) Wakayama MJ precipitation and the Niño 3.4 index (Trenberth and Stepaniak, 2001). Orange and black solid lines indicate the correlation coefficients of lag 0-year and lag 1-year, respectively. (c) Wavelet coherence between Wakayama MJ precipitation and the Niño 3.4 index (Trenberth and Stepaniak, 2001). Black contour means the 95% significant level, and white shade corresponds the cone of influence. Arrows mean the relative phase relation. (d) 31-year running variances for the normalized Niño 3.4 index (Trenberth and Stepaniak, 2001). (e) Instrumental spring (March–May) PDO index. Green solid line indicates 11 year moving average.

6-4. Summary

Time- and frequency-domain comparison between tree-ring cellulose $\delta^{18}O$ and various ENSO reconstructions indicates that teleconnection are strongest during the mid-17th, late 18th and late 19th centuries. Similar analysis of instrumental precipitation in central Japan shows a similar relationship since 1980. The ENSO-EASM teleconnection appears when ENSO variance is high, and this relationship may relate to the PDO phase.

Chapter 7

General discussion and future perspectives

7-1. General discussion

As summarized in chapter 1, the possible mechanisms of East Asian rainfall patterns during the last millennium were proposed in Chen et al. (2015). Modern observation identified that the intensity and position of Western Pacific Subtropical High (WPSH) potentially play an important role in modulating the relation between precipitation in eastern China and ENSO. During El Niño years, westward intensification and extension were observed in the WPSH, and this also shifted southward (Qian et al., 2007; Su and Xue, 2011). During this state, the rain-belt is not able to reach to North China relative to normal years. This can cause more precipitation in southern China (e.g., lower Yangtze River Catchment) and less precipitation in northern China. In La Niña years, intensity and position of the WPSH indicate weakening and northeastward retreat. Zhou and Yu (2005) suggested a smooth transport of moisture by low-level jet along the northwestern edge of the WPSH caused this response. On multi-centennial timescales, the similar patterns were observed in the reconstructed hydrological conditions during the last millennium (Fig. 7-1-1). Some previous studies identified that equatorial Pacific Ocean had La Niña (El Niño) like condition in the MCA (LIA) (e.g., Mann et al., 2009). This La Niña-like condition possibly causes more precipitation in northern China and less precipitation in southern China. During the LIA, a contrasting rainfall pattern was observed due to El Niño-like condition. However, Chen et al. (2015) mentioned that as of now there are not enough proxy records in eastern China and the surroundings to discuss about the detail discussion about this asynchronous variability. Hydrological reconstructions in central Japan may shed light on this issue, because the EOF analysis based on the annual precipitation during the modern period (AD 1900–2008) indicates the clear rainfall pattern (Fig. 7-1-2). Rainfall pattern analysis for the modern period (AD 1900–2008) also indicated that this proposal was not able to explain the long-term precipitation increase in Nansei Islands including Yakushima Island. To understand long-term precipitation trends regarding this issue, hydrological reconstruction is needed in Yakushima Island. Furthermore, different mechanisms can influence on the East Asian climate variability on annual and inter-annual time scales. ENSO had a potentially important controlling factor for the EASM in these time scales, and proxy-based environmental reconstructions are needed to better understand the longer-term

inter-annual relationship of the ENSO-EASM teleconnection.

My tree-ring cellulose $\delta^{18}O$ chronologies from central Japan and Yakushima Island provided the important information for the hypothesis of Chen et al. (2015). On multi-centennial timescales, my datasets from central Japan showed that the tree-ring cellulose $\delta^{18}O$ values were relatively low during the LIA, suggesting that the hydrological condition was wet in this cold period (chapter 2). Data from Yakushima Island indicated that the $\delta^{18}O$ values were relatively low (high) during the MCA (LIA), and this may indicate that the early summer precipitation increased (decreased) in the warm (cold) period (chapter 3). Assuming that the hydrological conditions during the LIA have similar changes relative to both the MCA and current warm period, my tree-ring cellulose $\delta^{18}O$ data from central Japan indicate the opposite hydroclimate change from that of Yakushima Island. My analyses suggest that this may relate to the different correlation with SST around the western North Pacific SST (chapter 4 and 5). On annual and inter-annual time scales, the relationship of the ENSO-EASM has multidecadal variability and this teleconnection appears clear when ENSO variance is high (chapter 6).

Based on these findings, here, I compared the tree-ring cellulose $\delta^{18}O$ chronology in central Japan with the spatial pattern of hydrological conditions during the past millennium (Fig. 7-1-1). Assuming that the hydrological conditions during the LIA have the similar changes relative to both the MCA and modern warm period, my datasets suggest that the hydroclimate in central Japan was wet in the LIA. The wetness map including these reconstructions is consistent with the averaged mode of annual precipitation during the past 100 years (Fig. 7-1-2). This supports the idea that the mean state of the Pacific ocean-atmospheric system currently observed has been also dominant over the past millennium (Chen et al., 2015).

Similar comparisons were also performed for Yakushima tree-ring $\delta^{18}O$. In Yakushima Island, 19-year averaged MJ precipitation shows the increasing trend from AD 1947 to 2004 (Fig. 7-1-3). This observation data suggests that the mean state of precipitation in this region indicate the positive EOF mode in Fig. 7-1-2. Assuming that tree-ring cellulose $\delta^{18}O$ is mainly controlled by amount effect, the early summer precipitation in Yakushima Island increased (decreased) during the MCA (LIA). Proposal of Chen et al. (2015) was not able to explain this long-term variability in Yakushima Island. Comparisons between my data and global SSTs suggest that SST

variability in the western North Pacific plays an important role in the hydroclimate in Yakushima Island. Based on this analysis, I propose that this relates to changes of the Kuroshio Current.

Tropical Pacific SST reconstructions support the idea from Chen et al., (2015). The eastern (western) equatorial Pacific was cooler (warmer) during the MCA (Oppo et al., 2009; Conroy et al., 2009; Fig. 7-1-4). This state of La Niña like condition leads to the hydrological conditions shown in Fig. 7-1-1. The El Niño like condition is also observed in the tropical Pacific SST reconstructions during the LIA (Fig. 7-1-4). This contrast could have caused the opposite hydroclimate changes during this cold period relative to MCA.

In northern Japan, the long-term hydrological variability is similar to that of central Japan. Sun et al. (2015) present regional hydroclimate reconstruction in Hokkaido during the past 400 years. Their sediment core δ^{15}N record from Lake Onuma (Fig. 7-1-5) revealed the long-term hydrological variability. Their reconstruction indicated that the precipitation gradually increased from mid 17th century and reached maximum around mid 19th century (Sun et al., 2015; Fig. 7-1-6). During the 20th century, their results showed dry condition in Hokkaido. This long-term trend is synchronized with my tree-ring cellulose δ^{18}O data in central Japan. Thus, this comparison suggests that the hydrological conditions in central and northern Japan have same centennial variability over the past four centuries.

Previous work using meteorological data suggests that the ITCZ shifts southward when westward extension and southward shift are observed in the WPSH (e.g., Lu and Dong, 2001). To confirm this relationship between the ITCZ and WPSH over the past millennium, I compared the long-term hydrological variability in East Asia with the reconstruction of ITCZ position. Sachs et al. (2009) presents the mean position of ITCZ over the past millennium. Their three lake sediment records from equatorial Pacific indicate that the ITCZ was south of its modern position during the LIA (Sachs et al., 2009). Chen et al. (2015) proposes that the WPSH extended westward and shifted southward during the El Niño like condition in the LIA period. Based on meteorological analysis for the relationship between the ITCZ and WPSH (e.g., Lu and Dong, 2001), this southward movement of ITCZ is consistent with the proposed WPSH movement over the past millennium (Chen et al., 2015).

As summarized in this chapter, my tree-ring cellulose $\delta^{18}O$ datasets suggest that Japanese hydrological conditions are mainly controlled by the long-term SST variability on multi-centennial time scale. On the other hand, different mechanisms can influence the East Asian climate variability on annual and inter-annual time scales. My time- and frequency-domain comparison between tree-ring cellulose $\delta^{18}O$ in central Japan and ENSO reconstructions indicates that teleconnection are strongest when ENSO variance is high, and this relationship may relate to the PDO phase. These findings propose that different mechanisms existed in East Asia on various time scales. In this dissertation, I showed that tree-ring cellulose $\delta^{18}O$ is a powerful tool to develop understanding about the possible mechanisms of both high- and low-frequency hydrological variations in Japan.

インターネット公表に関する同意が
得られなかったため非公表

Fig. 7-1-1. Map showing the hydrological conditions during the MCA and LIA (Chen et al., 2015). These reconstructed conditions were categorized into dry, moderate and wet. Minus and plus symbols indicate moderately dry and moderately wet, respectively.

インターネット公表に関する同意が
得られなかったため非公表

Fig. 7-1-2. EOF1 pattern based on the annual precipitation during the AD 1900–2008 (Chen et al., 2015). The values indicate the eigenvectors of EOF1 mode.

インターネット公表に関する共著者全員の
同意が得られていないため、
本章の一部については、非公開

Fig. 7-1-3. 19-year averaged MJ precipitation at Yakushima station from AD 1947 to 2004.

インターネット公表に関する共著者全員の
同意が得られていないため、
本章の一部については、非公開

Fig. 7-1-4. (a) Mie tree-ring cellulose δ^{18}O chronology (AD 1600–1959; blue) and MJJ relative humidity at Tsu station (1890–2013; dark green). Gray shading indicates the uncertainty period in the long-term hydroclimate reconstruction. (b) Tree-ring δ^{18}O at Yakushima Island. Thick black lines indicate 19-year moving averages. (c) SST reconstruction in the western equatorial Pacific (Oppo et al., 2009). (d) Diatom T/E index in the eastern equatorial Pacific (Conroy et al., 2009).

インターネット公表に関する同意が

得られなかったため非公表

Fig. 7-1-5. Map showing the site of Lake Onuma (Sun et al., 2015).

インターネット公表に関する同意が

得られなかったため非公表

Fig. 7-1-6. $\delta^{15}N$ in Lake Onuma over the past four centuries (modified from Sun et al., 2015).

7-2. Future perspectives

7-2-1. Climate reconstructions

In this dissertation, I presented tree-ring growth rates in Yakushima Island (chapter 3). This allowed me to consider that the cedar trees in this study site mainly grew from May to June. In chapter 2 and 3, I investigated the typhoon influences on the tree-ring cellulose $\delta^{18}O$ values of Japanese cedars in both central Japan and Yakushima Island. This is because the precipitation $\delta^{18}O$ value related to tropical typhoons is extremely low (e.g., Lawrence and Gedzelman, 1996). My comparisons indicated that there are no clear relationships between cedar tree-ring cellulose $\delta^{18}O$ and the number of typhoons. I suggest that it is possibly because Japanese cedar trees do not grow during typhoon seasons.

Li et al. (2015) reported that tree-ring cellulose $\delta^{18}O$ in pine and oak from central Japan potentially recorded the past typhoon events. The highest correlations between cellulose $\delta^{18}O$ and meteorological data propose the main growth periods of these trees, and the intervals may overlap the typhoon events in late summer. However, observations of tree-ring growth rates, especially main tree-ring growth intervals, are necessary to confirm this high correlation (chapter 3). This validation for various tree species would enable me to develop hydroclimate reconstructions using tree-ring cellulose $\delta^{18}O$. For example, I should identify some specific trees, which mainly grow in the late summer. Measurements of cellulose $\delta^{18}O$ for this species may allow reconstructions of past typhoon events. Identification of trees that mainly grow from June to August potentially enables me to provide a proxy-based PJ pattern index. As mentioned in Chapter 1, a previous study has presented a 117-year PJ pattern index using JJA station pressure data from Yokohama and Hengchun of Taiwan (Kubota et al., 2015). This index revealed that the relationship between ENSO and PJ pattern has interdecadal variability. Comparison between tree-ring $\delta^{18}O$ using this species in central Japan and Taiwan potentially allow me to provide the longer index of PJ pattern than available instrumental records. This proxy-based long index may shed light on the interannual changes of summer atmospheric–ocean circulation.

7-2-2. Toward the validation for climate model performance

Comparisons between simulated and reconstructed rainfall pattern during the past millennium are necessary to project long-term future precipitation change in IPCC. In this section, I show the comparisons of my tree-ring $\delta^{18}O$ chronologies with simulated precipitations.

As summarized in Section 1, the simulated rainfall patterns, except for the results of Man et al. (2012), mostly show dry conditions (Liu et al., 2009; Zhou et al., 2011; Yan et al., 2015) in Japan during the LIA relative to MCA/modern 150 years. In the models of Liu et al. (2009) and Zhou et al. (2011), they considered solar variability, volcanic activity, and greenhouse gases as the external factors. Man et al. (2012) used land cover change in addition to these three external factors. Yan et al. (2015) presented the simulated precipitation by using only the total solar irradiance (TSI) as an external forcing. Simulated precipitation using the three external factors (Liu et al., 2009; Zhou et al., 2011) and only the TSI (Yan et al., 2015) revealed a relatively dry climate in central Japan during the LIA. Conversely, my relative humidity reconstruction in central Japan showed a wet climate during the LIA, which may indicate that these climate models could not reproduce the hydrological climate in central Japan precisely. The climate model that used four external factors (solar variability, volcanic activity, greenhouse gases, and land cover change) did reproduce a wet climate in central Japan during the LIA (Man et al., 2012) (Fig 7-2-1). However, this climate model produced discrepancies over eastern China (Zhang et al., 2008) and Yakushima Island (this study).

These comparisons suggest that my hydrological reconstructions using tree-ring cellulose $\delta^{18}O$ allow me to validate the long-term performance of climate models over the past millennium. CMIP 5 showed that the agreements among models are less than 66% for future mean spring precipitation in East Asia from AD 2045 to 2065 (Collins et al., 2013) (Fig 7-2-2). In the summer season, there are only few areas where more than 90% of the results from models agree each other (Fig 7-2-3). Although the relatively short instrumental records hinder the validation for the long-term performance of the climate models, my annually resolved hydrological reconstructions may shed light on this issue.

140

インターネット公表に関する同意が
得られなかったため非公表

Fig 7-2-1. Anomalies of summer precipitation and 850-hPa winds during the LIA (Man et al., 2012). These anomalies relative to the last millennial average are drawn by colored shading (mm/day). The vectors indicate the 850-hPa winds (m/s). Black dots indicate the 95% significant areas.

インターネット公表に関する同意が
得られなかったため非公表

Fig. 7-2-2. CMIP5 average percentage change in mean spring (MAM) precipitation during the period from AD 2045 to 2065 under the RCP8.5 forcing scenario (IPCC, 2013). The reference period is from AD 1986 to 2005. Hatching regions show that the mean change of multi-model is less than one standard deviation. Stippling indicates areas where more than 90% of the models agree on.

インターネット公表に関する同意が
得られなかったため非公表

Fig. 7-2-3. Same as Fig 1-2-22, except for mean summer (JJA) precipitation (IPCC, 2013).

7-3. Conclusion

In this dissertation, validations for tree-ring cellulose $\delta^{18}O$ in Japan are presented. First, two long cedar tree-ring $\delta^{18}O$ datasets from central Japan allow consideration that this proxy is able to reconstruct the long-term hydroclimate variability (chapter 2). Second, observations of tree-ring growth rates and meteorological data in Yakushima Island increase a reliability of hydrological reconstruction using tree-ring cellulose $\delta^{18}O$ (chapter 3). Based on these examinations, I discussed about the possible influence of the equatorial Pacific SST on the long-term hydroclimate variations in central Japan (Chapter 4). In Yakushima Island, my analysis suggests that the Kuroshio Current plays an important role in the hydroclimate changes (Chapter 5). In Chapter 6, I investigated long-term changes in inter-annual relationship between ENSO and tree-ring cellulose $\delta^{18}O$ in central Japan. In the final chapter, my discussions could develop an understanding of the mechanism for the long-term rainfall pattern in eastern part of East Asia (chapter 7). The key findings are summarized in this section.

(1) *Japanese cedar trees are suitable to reconstruct long-term hydroclimate variability, except for the $\delta^{18}O$ values of inner cedar.*

Measurements of cellulose $\delta^{18}O$ were performed for two long cedar trees from central Japan. These two chronologies allowed me to consider the age-related trend of Japanese cedars from central Japan. Regression lines for tree-ring $\delta^{18}O$ indicated that there were no significant age-related trends in the cedar trees, except for the $\delta^{18}O$ values of inner cedar.

(2) *Observations of meteorological data and tree-ring growth rates can increase reliability of hydroclimate reconstruction using tree-ring cellulose $\delta^{18}O$.*

I reported Yakushima tree-ring cellulose $\delta^{18}O$. In this site, my observations of tree-ring growth rates and meteorological data allowed me to confirm a reliability of reconstructions using tree-ring cellulose $\delta^{18}O$. Correlation analyses were performed for meteorological data. This analyses indicated that Yakushima tree-ring cellulose $\delta^{18}O$ significantly correlated with May–June (MJ) precipitation. My observations of

meteorological data and tree-ring growth rates agreed with these validations.

(3) *SST variability in the equatorial Pacific played an important role in the long-term hydrological conditions in central Japan.*

I reconstructed long-term hydroclimate variability from AD 1600 to 1959 by using tree-ring cellulose $\delta^{18}O$ from central Japan. Comparisons between my relative humidity reconstruction and global SSTs suggested that SST variability in the equatorial Pacific played an important role in the hydrological conditions of central Japan.

(4) *The Kuroshio Current played an important role in long-term Yakushima hydroclimate changes.*

I presented Yakushima tree-ring cellulose $\delta^{18}O$ chronology from AD 1025 to 1805. Assuming that this $\delta^{18}O$ variation mainly caused by amount effect, my data indicated that the precipitation decreased during the LIA relative to the MCA. Meteorological precipitation data and my tree-ring cellulose $\delta^{18}O$ synchronized with SST variations around the western North Pacific, suggesting that the Kuroshio Current played an important role in this hydroclimate changes.

(5) *On annual and inter-annual time scale, the ENSO-EASM relationship varies on multi-decadal time scale.*

Time- and frequency-domain comparison between my tree-ring cellulose $\delta^{18}O$ and ENSO reconstructions indicates that teleconnection are strongest during the mid-17th, late 18th and late 19th centuries. Similar analysis of instrumental precipitation in central Japan shows a similar relationship since 1980. The ENSO-EASM teleconnection appears when ENSO variance is high, and this relationship may relate to the PDO phase.

Acknowledgements

Citations to previously published work

Chapters 2 and 6 (with Appendix of chapter 6) has been published in its entirety in the following paper [Sakashita et al., 2015].

Sakashita, W., Y. Yokoyama, H. Miyahara, Y. T. Yamaguchi, T. Aze, S. P. Obrochta, and T. Nakatsuka (2015), Relationship between early summer precipitation in Japan and the El Niño-Southern and Pacific Decadal Oscillations over the past 400 years, *Quaternary International*, doi:10.1016/j.quaint.2015.05.054.

References

Aono, Y., and K. Kazui (2008), Phenological data series of cherry tree flowering in Kyoto, Japan, and its application to reconstruction of springtime temperatures since the 9th century, *Int. J. Climatol.*, *28*(7), 905–914, doi:10.1002/joc.1594.

Braganza, K., J. L. Gergis, S. B. Power, J. S. Risbey, and A. M. Fowler (2009), A multiproxy index of the El Niño–Southern Oscillation, A.D. 1525–1982, *J. Geophys. Res.*, *114*, D05106, doi:10.1029/2008JD010896.

Burk, R., and M. Stuiver (1981), Oxygen isotope ratios in trees reflect mean annual temperature and humidity, *Science, 211*, 1417–1419.

Chan, J. C. L. and Zhou (2005), PDO, ENSO and the early summer monsoon rainfall over south China, *Geophys. Res. Lett.*, *32*(8), L08810, doi:10.1029/2004GL022015.

Chen, J., F. Chen, S. Feng, W. Huang, J. Liu, and A. Zhou (2015), Hydroclimatic changes in China and surroundings during the Medieval Climate Anomaly and Little Ice Age: spatial patterns and possible mechanisms, *Quat. Sci. Rev.*, *107*, 98–111, doi:10.1016/j.quascirev.2014.10.012.

Chu, G. et al. (2002), The 'MedievalWarm Period' drought recorded in Lake Huguangyan, tropical South China. Holocene **12,** 511–516.

Cobb, K., C. Charles, H. Cheng, and R. Edwards (2003), El Niño/Southern Oscillation and tropical Pacific climate during the last millennium, *Nature*, *424*, 271–276.

Cobb, K. M., N. Westphal, H. R. Sayani, J. T. Watson, E. Di Lorenzo, H. Cheng, R. L. Edwards, and C. D. Charles (2013), Highly variable El Niño-Southern Oscillation throughout the Holocene., *Science*, *339*(6115), 67–70, doi:10.1126/science.1228246.

Collins M, Knutti R, Arblaster JM et al. (2013) Chapter 12: Long-term Climate Change: Projections, Commitments and Irreversibility. In: Working Group I Contribution to the IPCC Fifth Assessment Report (AR5), Climate Change 2013: The Physical Science Basis. Cambridge University Press, Cambridge.

Conroy, J. L., A. Restrepo, J. T. Overpeck, M. Steinitz-Kannan, J. E. Cole, M. B. Bush, and P. a. Colinvaux (2008), Unprecedented recent warming of surface

temperatures in the eastern tropical Pacific Ocean, *Nat. Geosci.*, *2*, 46–50, doi:10.1038/ngeo390.

Cook, E. R., K. J. Anchukaitis, B. M. Buckley, R. D. D'Arrigo, G. C. Jacoby, and W. E. Wright (2010), Asian monsoon failure and megadrought during the last millennium., *Science*, *328*, 486–489, doi:10.1126/science.1185188.

Cook, E. R., P. J. Krusic, K. J. Anchukaitis, B. M. Buckley, T. Nakatsuka, and M. Sano (2013), Tree-ring reconstructed summer temperature anomalies for temperate East Asia since 800 C.E., *Clim. Dyn.*, *41*, 2957–2972, doi:10.1007/s00382-012-1611-x.

Craig, H., and L. I. Gordon (1965), *Deuterium and Oxygen 18 Variations in the Ocean and the Marine Atmosphere,* Consiglio nazionale delle richerche, Laboratorio de geologia nucleare, Pisa, Italy.

Crowley, T., S. Obrochta, and J. Liu (2014), Recent global temperature " plateau " in the context of a new proxy reconstruction, *Earth's Futur.*, 281–294, doi:10.1002/2013EF000216.Abstract.

D'Arrigo, R., and R. Wilson (2006), On the Asian expression of the PDO, *Int. J. Climatol.*, *26*(12), 1607–1617, doi:10.1002/joc.1326.

Dansgard, W. (1964), Stable isotopes in precipitation, *Tellus*, *16*, 436–468.

Denniston, R. F. et al. (2013), A Stalagmite record of Holocene Indonesian–Australian summer monsoon variability from the Australian tropics, *Quat. Sci. Rev.*, *78*, 155–168, doi:10.1016/j.quascirev.2013.08.004.

Dongmann, G., H. W. Nürnberg, H. Förstel, and K. Wagener (1974), On the enrichment of $H_2^{18}O$ in the leaves of transpiring plants, Radiat. Environ.Biophys., 11, 41–52, doi:10.1007/BF01323099.

Eddy, J. A. (1976), The Maunder Minimum, *Science*, *192*, 1189–1202, doi:10.1126/science.192.4245.1189.

Esper, J., D. C. Frank, G. Battipaglia, U. Büntgen, C. Holert, K. Treydte, R. Siegwolf, and M. Saurer (2010), Low-frequency noise in δ 13 C and δ 18 O tree ring data: A case study of Pinus uncinata in the Spanish Pyrenees, *Global Biogeochem. Cycles*, *24*(4), GB4018, doi:10.1029/2010GB003772.

Farquhar, G. D., K. T. Hubick, A. G. Condon, and R. A. Richards (1989), Carbon isotope fractionation and plant water-use efficiency, in Stable Isotopes in

Ecological Research, edited by P. W. Rundel, J. R. Ehleringer, and K. A. Nagy, pp. 21–40, Springer, New York, doi:10.1007/978-1-4612-3498-2_2.

Feng, J., L. Wang, and W. Chen (2014), How Does the East Asian Summer Monsoon Behave in the Decaying Phase of El Niño during Different PDO Phases?, *J. Clim.*, *27*(7), 2682–2698, doi:10.1175/JCLI-D-13-00015.1.

Ghil, M. et al. (2002), Advanced spectral methods for climatic time series, *Rev. Geophys.*, *40*(1), 1003, doi:10.1029/2000RG000092.

Grinsted, A., J. C. Moore, and S. Jevrejeva (2004), Application of the cross wavelet transform and wavelet coherence to geophysical time series, *Nonlinear Process. Geophys.*, *11*, 561–566.

Hu, C., G. M. Henderson, J. Huang, S. Xie, Y. Sun, and K. R. Johnson (2008), Quantification of Holocene Asian monsoon rainfall from spatially separated cave records, *Earth Planet. Sci. Lett.*, *266*(3-4), 221–232, doi:10.1016/j.epsl.2007.10.015.

IPCC (2013), Summary for policymakers, in *Climate Change 2013: The Physical Science Basis. Contribution of Working Group I to the Fifth Assessment Report of the Intergovernmental Panel on Climate Change*, edited by T. F. Stocker et al., Cambridge Univ. Press, Cambridge, U. K., and New York.

Johnstone, J. a., J. S. Roden, and T. E. Dawson (2013), Oxygen and carbon stable isotopes in coast redwood tree rings respond to spring and summer climate signals, *J. Geophys. Res. Biogeosciences*, *118*(4), 1438–1450, doi:10.1002/jgrg.20111.

Kawabe, M. (1995), Variations of Current Path, Velocity, and Volume Transport of the Kuroshio in Relation with the Large Meander, *J. Phys. Oceanogr.*, *25*(12), 3103–3117, doi:10.1175/1520-0485(1995)025<3103:VOCPVA>2.0.CO;2.

Kawamura, K. et al. (2007), Northern Hemisphere forcing of climatic cycles in Antarctica over the past 360,000 years., *Nature*, *448*(7156), 912–6, doi:10.1038/nature06015.

Kubota, H., Y. Kosaka, and S.-P. Xie (2015), A 117-year long index of the Pacific-Japan pattern with application to interdecadal variability, *Int. J. Climatol.*, doi:10.1002/joc.4441.

Kurita, N., Y. Fujiyoshi, T. Nakayama, Y. Matsumi, and H. Kitagawa (2015), East Asian Monsoon controls on the inter-annual variability in precipitation isotope ratio in Japan, *Clim. Past*, *11*(2), 339–353, doi:10.5194/cp-11-339-2015.

Lawrence, R., and D. Gedzelman (1996), Low stable isotope ratios of tropical cyclone rains, *Geophys. Res. Lett.*, *23*(5), 527–530.

Li, J., S.-P. Xie, E. R. Cook, G. Huang, R. D'Arrigo, F. Liu, J. Ma, and X.-T. Zheng (2011), Interdecadal modulation of El Niño amplitude during the past millennium, *Nat. Clim. Chang.*, *1*(2), 114–118, doi:10.1038/nclimate1086.

Li, J. et al. (2013), El Niño modulations over the past seven centuries, *Nat. Clim. Chang.*, *3*(9), 822–826, doi:10.1038/nclimate1936.

Li, Y., N. Wang, X. Zhou, C. Zhang, and Y. Wang (2014), Synchronous or asynchronous Holocene Indian and East Asian summer monsoon evolution: A synthesis on Holocene Asian summer monsoon simulations, records and modern monsoon indices, *Glob. Planet. Change*, *116*, 30–40, doi:10.1016/j.gloplacha.2014.02.005.

Li, Z., T. Nakatsuka, and M. Sano (2015), Tree-ring cellulose $\delta^{18}O$ variability in pine and oak and its potential to reconstruct precipitation and relative humidity in central Japan, *Geochem. J.*, *49*(2), 125–137, doi:10.2343/geochemj.2.0336.

Libby, L. M., L. J. Pandolfi, P. H. Payton, J. Marshall, B. Becker, and V. Giertz-Sienbenlist (1976), Isotopic tree thermometers, *Nature*, *261*(5558), 284–288, doi:10.1038/261284a0.

Liu, J., B. Wang, Q. Ding, X. Kuang, W. Soon, and E. Zorita (2009), Centennial Variations of the Global Monsoon Precipitation in the Last Millennium: Results from ECHO-G Model, *J. Clim.*, *22*(9), 2356–2371, doi:10.1175/2008JCLI2353.1.

Liu, J., B. Wang, H. Wang, X. Kuang, and R. Ti (2011a), Forced response of the East Asian summer rainfall over the past millennium: results from a coupled model simulation, *Clim. Dyn.*, *36*, 323–336, doi:10.1007/s00382-009-0693-6.

Liu, J., F. Chen, J. Chen, D. Xia, Q. Xu, Z. Wang, and Y. Li (2011b), Humid medieval warm period recorded by magnetic characteristics of sediments from Gonghai Lake, Shanxi, North China, *Chinese Sci. Bull.*, *56*(23), 2464–2474, doi:10.1007/s11434-011-4592-y.

Loader, N. J., I. Robertson, A. C. Barker, V. R. Switsur, and J. S. Waterhouse (1997), An improved technique for the batch processing of small wholewood samples to α-cellulose, *Chem. Geol.*, *136*(3-4), 313–317, doi:10.1016/S0009-2541(96)00133-7.

Loader, N. J., I. Robertson, and D. McCarroll (2003), Comparison of stable carbon isotope ratios in the whole wood, cellulose and lignin of oak tree-rings, *Palaeogeogr. Palaeoclimatol. Palaeoecol.*, *196*(3-4), 395–407, doi:10.1016/S0031-0182(03)00466-8.

Lu, R., and B. Dong (2001), Westward extension of North Pacific subtropical high in summer, *J. Meteorol. Soc. Japan*, *79*, 1229–1241.

Maejima, I., and Y. Tagami (1983), Climate of the Little Ice Age in Japan, *Geogr. Reports Tokyo Metrop. Univ.*, *18*, 91–111.

Majoube, M. (1971), Fractionnement en oxygen-18 et en deuterium entre l'eau et sa vapeur, J. Chim. Phys., 68, 1423–1436.

Man, W., T. Zhou, and J. H. Jungclaus (2012), Simulation of the East Asian Summer Monsoon during the Last Millennium with the MPI Earth System Model, *J. Clim.*, *25*(22), 7852–7866, doi:10.1175/JCLI-D-11-00462.1.

Mann, M. E., Z. Zhang, M. K. Hughes, R. S. Bradley, S. K. Miller, S. Rutherford, and F. Ni (2008), Proxy-based reconstructions of hemispheric and global surface temperature variations over the past two millennia., *Proc. Natl. Acad. Sci. U. S. A.*, *105*(36), 13252–7, doi:10.1073/pnas.0805721105.

Mann, M., R. Bradley, and M. Hughes (1998), Global-scale temperature patterns and climate forcing over the past six centuries, *Nature*, 779–788.

Mann, M. E. (2002), Little Ice Age, in *Encycl. Glob. Environ. Chang. Ed. by M. C. MacCracken J. S. Perry*, pp. 504–509, John Wiley, Chichester, U. K.

Mann, M. E., Z. Zhang, S. Rutherford, R. S. Bradley, M. K. Hughes, D. Shindell, C. Ammann, G. Faluvegi, and F. Ni (2009), Global signatures and dynamical origins of the Little Ice Age and Medieval Climate Anomaly., *Science*, *326*(5957), 1256–60, doi:10.1126/science.1177303.

Mantua, N. J., Hare, S. R., Zhang, Y., Wallace, J. M., Francis, R. C. (1997), A Pacific Interdecadal Climate Oscillation with Impacts on Salmon Production, *Bull. Am. Meteorol. Soc.*, *78*, 1069–1079.

Marcott, S. A., J. D. Shakun, P. U. Clark, and A. C. Mix (2013), A reconstruction of regional and global temperature for the past 11,300 years., *Science*, *339*(6124), 1198–201, doi:10.1126/science.1228026.

Masson-Delmotte, V., et al. (2013), Information from paleoclimate archives, in *Climate Change 2013: The Physical Science Basis. Contribution of Working Group I to the Fifth Assessment Report of the Intergovernmental Panel on Climate Change*, edited by T. F. Stocker et al., Cambridge Univ. Press, Cambridge, U. K., and New York.

McCarroll, D., and N. J. Loader (2004), Stable isotopes in tree rings, *Quat. Sci. Rev.*, *23*(7-8), 771–801, doi:10.1016/j.quascirev.2003.06.017.

McGregor, H. V., and M. K. Gagan (2004), Western Pacific coral δ 18 O records of anomalous Holocene variability in the El Niño–Southern Oscillation, *Geophys. Res. Lett.*, *31*(11), L11204, doi:10.1029/2004GL019972.

McGregor, H. V., M. J. Fischer, M. K. Gagan, D. Fink, S. J. Phipps, H. Wong, and C. D. Woodroffe (2013), A weak El Niño/Southern Oscillation with delayed seasonal growth around 4,300 years ago, *Nat. Geosci.*, *6*(11), 949–953, doi:10.1038/ngeo1936.

Miyahara, H., K. Masuda, and Y. Muraki (2004), CYCLICITY OF SOLAR ACTIVITY DURING THE MAUNDER MINIMUM DEDUCED FROM RADIOCARBON CONTENT, *Sol. Phys.*, (2004), 317–322.

Miyake, F., K. Nagaya, K. Masuda, and T. Nakamura (2012), A signature of cosmic-ray increase in AD 774-775 from tree rings in Japan., *Nature*, *486*(7402), 240–2, doi:10.1038/nature11123.

Nakamura, A. et al. (2015), Weak monsoon event at 4.2 ka recorded in sediment from Lake Rara, Himalayas, *Quat. Int.*, doi:10.1016/j.quaint.2015.05.053.

Nakatsuka, T., K. Ohnishi, and T. Hara (2004), Oxygen and carbon isotopic ratios of tree-ring cellulose in a conifer-hardwood mixed forest in northern Japan, *Geochem. J.*, *38*, 77–88.

Nakatsuka, T. (2007), Reconstruction of paleo-climate using tree-ring oxygen isotopic ratios, Low Temp. Sci., 65, 49–56. [in Japanese, with English abstract]

Nitta, T. (1987), Convective activities in the tropical western Pacific and their impact on the Northern Hemisphere summer circulation, *J. Meteorol. Soc. Japan*, *65*, 373–390.

Ogura, Y. (1999), General Meteorology, second edition, University of Tokyo press, ISBN4-13-062706-6

Ohyama, M., H. Yonenobu, J.-N. Choi, W.-K. Park, M. Hanzawa, and M. Suzuki (2013), Reconstruction of northeast Asia spring temperature 1784–1990, *Clim. Past*, *9*(1), 261–266, doi:10.5194/cp-9-261-2013.

Oppo, D. W., Y. Rosenthal, and B. K. Linsley (2009), 2,000-year-long temperature and hydrology reconstructions from the Indo-Pacific warm pool., *Nature*, *460*(7259), 1113–6, doi:10.1038/nature08233.

Osborne, M. C., R. B. Dunbar, D. a. Mucciarone, E. Druffel, and J.-A. Sanchez-Cabeza (2014), A 215-yr coral δ18O time series from Palau records dynamics of the West Pacific Warm Pool following the end of the Little Ice Age, *Coral Reefs*, *33*(3), 719–731, doi:10.1007/s00338-014-1146-1.

Qian, W., X. Lin, Y. Zhu, Y. Xu, and J. Fu (2007), Climatic regime shift and decadal anomalous events in China, *Clim. Change*, *84*(2), 167–189, doi:10.1007/s10584-006-9234-z.

Qin, J., Yuan, D., Lin, Y., Zhang, H., Zhang, M., Cheng, H., Wang, H., Yang, Y., Ran, J., (2008). High resolution stalagmite records of climate change since 800 a AD in Libo, Guizhou. Carsol. Sin. 27, 266–272. [in Chinese with English abstract]

Ramesh, R., S. Bhattacharya, and K. Gopalan (1986), Climatic correlations in the stable isotope records of silver fir (Abies pindrow) trees from Kashmir , India, *Earth Planet. Sci. Lett.*, *79*, 66–74.

Roden, J. S., G. Lin, and J. R. Ehleringer (2000), A mechanistic model for interpretation of hydrogen and oxygen isotope ratios in tree-ring cellulose, *Geochim. Cosmochim. Acta*, *64*(1), 21–35, doi:10.1016/S0016-7037(99)00195-7.

Rodysill, J. R., J. M. Russell, S. D. Crausbay, S. Bijaksana, M. Vuille, R. L. Edwards, and H. Cheng (2013), A severe drought during the last millennium in East Java, Indonesia, *Quat. Sci. Rev.*, *80*, 102–111, doi:10.1016/j.quascirev.2013.09.005.

Sachs, J. P., D. Sachse, R. H. Smittenberg, Z. Zhang, D. S. Battisti, and S. Golubic (2009), Southward movement of the Pacific intertropical convergence zone AD 1400–1850, *Nat. Geosci.*, *2*(7), 519–525, doi:10.1038/ngeo554.

Sano, M., C. Xu, and T. Nakatsuka (2012), A 300-year Vietnam hydroclimate and ENSO variability record reconstructed from tree ring δ 18 O, *J. Geophys. Res. Atmos.*, *117*, D12115, doi:10.1029/2012JD017749.

Sato, R., and Y. Suzuki (2010), Carbon and Nitrogen stable isotope analysis by EA/IRMS, *Res. Org. Geochem.*, *26*, 21–29.

Seino, H. (1993), An estimation of distribution of meteorological elements using GIS and AMeDAS data. J. Agr. Met. 48, 379–383 [in Japanese].

Smith, T. M., R. W. Reynolds, T. C. Peterson, and J. Lawrimore (2008), Improvements to NOAA's Historical Merged Land–Ocean Surface Temperature Analysis (1880–2006), *J. Clim.*, *21*(10), 2283–2296, doi:10.1175/2007JCLI2100.1.

Steinhilber, F. et al. (2012), 9,400 Years of Cosmic Radiation and Solar Activity From Ice Cores and Tree Rings., *Proc. Natl. Acad. Sci. U. S. A.*, *109*(16), 5967–71, doi:10.1073/pnas.1118965109.

Sternberg, L. S. L. (2009), Oxygen stable isotope ratios of tree-ring cellulose: the next phase of understanding, *New Phytol.*, *181*, 553–562.

Su, T., and F. Xue (2011), Two Northward Jumps of the Summertime Western Pacific Subtropical High and Their Associations with the Tropical SST Anomalies, *Atmos. Ocean. Sci. Lett*, *4*(2), 98–102.

Sun, W., J. Shen, E. Zhang, N. Hasebe, K. Kashiwaya, R. Chen, and T. Itono (2015), Stable nitrogen isotope record of lacustrine sediments in Lake Onuma (Northern Japan) indicates regional hydrological variability during the past four centuries, *Quat. Int.*, 1–10, doi:10.1016/j.quaint.2015.07.036.

Suzuki, Y., and R. Sato (2010), Stable hydrogen and oxygen isotope analysis of organic materials by thermal conversion elemental analyzer / isotope mass spectrometer, Res. Org. Geochem., 26, 31–37. [in Japanese, with English abstract]

Tan, L., Y. Cai, L. Yi, Z. An, and L. Ai (2008), Precipitation variations of Longxi , northeast margin of Tibetan plateau since AD 960 and its relationship with solar activity, *Clim. Past*, *4*, 19–28.

Tan, L., Y. Cai, Z. An, R. L. Edwards, H. Cheng, C.-C. Shen, and H. Zhang (2010), Centennial- to decadal-scale monsoon precipitation variability in the semi-humid region, northern China during the last 1860 years: Records from stalagmites in Huangye Cave, *The Holocene*, *21*(2), 287–296, doi:10.1177/0959683610378880.

Tierney, J. E., D. W. Oppo, Y. Rosenthal, J. M. Russell, and B. K. Linsley (2010), Coordinated hydrological regimes in the Indo-Pacific region during the past two millennia, *Paleoceanography*, *25*(1), PA1102, doi:10.1029/2009PA001871.

Tomita, T., H. Sato, M. Nonaka, and M. Hara (2007), Interdecadal variability of the early summer surface heat flux in the Kuroshio region and its impact on the Baiu frontal activity, *Geophys. Res. Lett.*, *34*(10), L10708, doi:10.1029/2007GL029676.

Torrence, C., and G. P. Compo (1998), A Practical Guide to Wavelet Analysis, *Bull. Am. Meteorol. Soc.*, *79*, 61–78.

Trenberth, K., and D. Stepaniak (2001), Indices of El Niño evolution, *J. Clim.*, 1697–1701.

Treydte, K. S., G. H. Schleser, G. Helle, D. C. Frank, M. Winiger, G. H. Haug, and J. Esper (2006), The twentieth century was the wettest period in northern Pakistan over the past millennium., *Nature*, *440*(7088), 1179–82, doi:10.1038/nature04743.

Wang, B., and H. Lin (2002), Rainy Season of the Asian – Pacific Summer Monsoon, *J. Clim.*, *15*, 386–398.

Wang, B., R. Wu, and X. Fu (2000), Pacific – East Asian Teleconnection: How Does ENSO Affect East Asian Climate?, *J. Clim.*, *13*, 1517–1536.

Wang, B., J. Yang, T. Zhou, and B. Wang (2008), Interdecadal Changes in the Major Modes of Asian–Australian Monsoon Variability: Strengthening Relationship with ENSO since the Late 1970s, *J. Clim.*, *21*(8), 1771–1789, doi:10.1175/2007JCLI1981.1.

Wang, Y., H. Cheng, R. Edwards, and Z. An (2001), A High-Resolution Absolute-Dated Late Pleistocene Monsoon Record from Hulu Cave , China, *Science (80-.).*, *294*, 2345–2348.

Wanner, H. et al. (2008), Mid- to Late Holocene climate change: an overview, *Quat. Sci. Rev.*, *27*(19-20), 1791–1828, doi:10.1016/j.quascirev.2008.06.013.

Wasson, R., Bayliss, P. & Clelland, S. in Symp. 4: Climate Change (ed.Winderlich, S.) Kakadu National Park Landscape Symposia Series 2007–2009, Internal Report 567 (Supervising Scientist Division, Australian Government, 2010).

Watanabe, O., J. Jouzel, S. Johnsen, F. Parrenin, H. Shoji, and N. Yoshida (2003), Homogeneous climate variability across East Antarctica over the past three glacial cycles., *Nature*, *422*(6931), 509–12, doi:10.1038/nature01525.

White, J., E. Cook, and J. Lawrence (1985), The DH ratios of sap in trees: Implications for water sources and tree ring DH ratios, *Geochim. Cosmochim. Acta*, *4*, 237–246.

Wolter, K., and M. S. Timlin (2011), El Niño/Southern Oscillation behaviour since 1871 as diagnosed in an extended multivariate ENSO index (MEI.ext), *Int. J. Climatol.*, *31*(7), 1074–1087, doi:10.1002/joc.2336.

Wu, R., and B. Wang (2002), A Contrast of the East Asian Summer Monsoon – ENSO Relationship between 1962–77 and 1978-93, *J. Clim.*, *15*, 3266–3279, doi:http://dx.doi.org/10.1175/1520-0442(2002)015<3266:ACOTEA>2.0.CO;2.

Wu, W., W. Tan, L. Zhou, H. Yang, and Y. Xu (2012), Sea surface temperature variability in southern Okinawa Trough during last 2700 years, *Geophys. Res. Lett.*, *39*(14), L14705, doi:10.1029/2012GL052749.

Xu, C., M. Sano, and T. Nakatsuka (2011), Tree ring cellulose δ 18 O of Fokienia hodginsii in northern Laos: A promising proxy to reconstruct ENSO?, *J. Geophys. Res. Atmos.*, *116*, D24109, doi:10.1029/2011JD016694.

Xu, C., M. Sano, and T. Nakatsuka (2013), A 400-year record of hydroclimate variability and local ENSO history in northern Southeast Asia inferred from tree-ring δ18O, *Palaeogeogr. Palaeoclimatol. Palaeoecol.*, *386*, 588–598, doi:10.1016/j.palaeo.2013.06.025.

Yamaguchi, Y. T., Y. Yokoyama, H. Miyahara, K. Sho, and T. Nakatsuka (2010), Synchronized Northern Hemisphere climate change and solar magnetic cycles during the Maunder Minimum., *Proc. Natl. Acad. Sci. U. S. A.*, *107*(48), 20697–702, doi:10.1073/pnas.1000113107.

Yan, H., L. Sun, D. W. Oppo, Y. Wang, Z. Liu, Z. Xie, X. Liu, and W. Cheng (2011), South China Sea hydrological changes and Pacific Walker Circulation variations over the last millennium., *Nat. Commun.*, *2*, 293, doi:10.1038/ncomms1297.

Yan, H., W. Wei, W. Soon, Z. An, W. Zhou, Z. Liu, Y. Wang, and R. M. Carter (2015), Dynamics of the intertropical convergence zone over the western Pacific during the Little Ice Age, *Nat. Geosci.*, *8*(4), 315–320, doi:10.1038/ngeo2375.

Yang, B., C. Qin, J. Wang, M. He, T. M. Melvin, T. J. Osborn, and K. R. Briffa (2014), A 3,500-year tree-ring record of annual precipitation on the northeastern Tibetan Plateau, *Proc. Natl. Acad. Sci.*, *111*(8), 2903–2908, doi:10.1073/pnas.1319238111.

Yi, L., H. Yu, J. Ge, Z. Lai, X. Xu, L. Qin, and S. Peng (2012), Reconstructions of annual summer precipitation and temperature in north-central China since 1470 AD based on drought/flood index and tree-ring records, *Clim. Change*, *110*, 469–498, doi:10.1007/s10584-011-0052-6.

Yim, S.-Y., B. Wang, and M. Kwon (2013), Interdecadal change of the controlling mechanisms for East Asian early summer rainfall variation around the mid-1990s, *Clim. Dyn.*, *42*(5-6), 1325–1333, doi:10.1007/s00382-013-1760-6.

Yokoyama, Y., T. Naruse, N. O. Ogawa, R. Tada, H. Kitazato, and N. Ohkouchi (2006), Dust influx reconstruction during the last 26,000 years inferred from a sedimentary leaf wax record from the Japan Sea, *Glob. Planet. Change*, *54*, 239–250, doi:10.1016/j.gloplacha.2006.06.022.

Yonenobu, H., and D. Eckstein (2006), Reconstruction of early spring temperature for central Japan from the tree-ring widths of Hinoki cypress and its verification by other proxy records, *Geophys. Res. Lett.*, *33*(10), L10701, doi:10.1029/2006GL026170.

Yoon, J., and S.-W. Yeh (2010), Influence of the Pacific Decadal Oscillation on the Relationship between El Niño and the Northeast Asian Summer Monsoon, *J. Clim.*, *23*(17), 4525–4537, doi:10.1175/2010JCLI3352.1.

Young, G. H. F., J. C. Demmler, B. E. Gunnarson, A. J. Kirchhefer, N. J. Loader, and D. McCarroll (2011), Age trends in tree ring growth and isotopic archives: A case study of Pinus sylvestris L. from northwestern Norway, *Global Biogeochem. Cycles*, *25*(2), GB2020, doi:10.1029/2010GB003913.

Zeng, Y. et al. (2011), The wet Little Ice Age recorded by sediments in Huguangyan Lake, tropical South China. Quat. Int. **263,** 55–62.

Zhang, P. et al. (2008), A test of climate, sun, and culture relationships from an 1810-year Chinese cave record., *Science (80-.).*, *322*(5903), 940–2, doi:10.1126/science.1163965.

Zhou, T.-J., and Ru-Cong Yu (2005), Atmospheric water vapor transport associated with typical anomalous summer rainfall patterns in China, *J. Geophys. Res.*, *110*(D8), D08104, doi:10.1029/2004JD005413.

Zhou, T., B. Li, W. Man, L. Zhang, and J. Zhang (2011), A comparison of the Medieval Warm Period, Little Ice Age and 20th century warming simulated by the FGOALS climate system model, *Chinese Sci. Bull.*, *56*(28-29), 3028–3041, doi:10.1007/s11434-011-4641-6.

Zhou, X., P. Zhao, G. Liu, and T. Zhou (2011), Characteristics of decadal-centennial-scale changes in East Asian summer monsoon circulation and precipitation during the Medieval Warm Period and Little Ice Age and in the present day, *Chinese Sci. Bull.*, *56*(28-29), 3003–3011, doi:10.1007/s11434-011-4651-4.

List of abbreviation

Abbreviation	Definition
AMJ	April–May–June
ASM	Australian Summer Monsoon
CMAP	CPC Merged Analysis of Precipitation
CMIP5	Coupled Model Intercomparison Project Phase 5
EASM	East Asian summer monsoon
ENSO	El Niño–Southern Oscillation
ERSST v3b	Extended Reconstructed SST version 3b
FGOALS	Flexible Global Ocean–Atmosphere–Land–Sea ice
GCM	General Circulation Model
IAEA	International Atomic Energy Agency
IPCC	Intergovernmental Panel on Climate Change
IRMS	Isotope ratio mass specttometry
ITCZ	Intertropical convergence zone
JJA	June–July–August
LGM	Last Glacial Maximum
LIA	Little Ice Age
MAM	March–April–May
MCA	Medieval Climate Anomaly
MJ	May–June
MJJ	May–June–July
MTM	Multitaper method
MWP	Medieval Warm Period
MXD	Maximum latewood density
MPI-ESM	Max Planck Institute Earth System Model
NCEP	National Centers for Environmental Prediction
NDJ	previous November–January
NH	Northern Hemisphere
ODP	Ocean drilling program
PDO	Pacific Decadal Oscillation

PDSI	Palmer Drought Severity Index
PJ pattern	Pacific Japan pattern
RCP	Representative Concentration Pathways
SST	Sea Surface Temperature
SSTA	Sea Surface Temperature Anomaly
TCEA	Thermal conversion elemental analyzer
TRW	Tree ring width
TSI	Total solar irradiance
VSMOW	Vienna Standard Mean Ocean Water
WNP	Western North Pacific
WPSH	Western Pacific Subtropical High

Appendix of chapter 2

インターネット公表に関する共著者全員の

同意が得られていないため、

本章の一部については、非公開

Fig. A2-1. Mie (Ise) tree-ring cellulose δ^{18}O and Tsu MJJ relative humidity time series. Blue and green solid lines indicate Mie tree-ring cellulose δ^{18}O and MJJ relative humidity at Tsu station, respectively.

Appendix of chapter 3

インターネット公表に関する共著者全員の

同意が得られていないため、

本章の一部については、非公開

Fig. A3-1. May precipitation comparison between Yakushima weather station (blue) and mesh grid points around tree-ring site.

インターネット公表に関する共著者全員の

同意が得られていないため、

本章の一部については、非公開

Fig. A3-2. Same as Fig. A3-1, except for June precipitation.

インターネット公表に関する共著者全員の
同意が得られていないため、
本章の一部については、 非公開

Fig. A3-3. Same as Fig. A3-1, except for July precipitation.

Appendix of chapter 5

インターネット公表に関する共著者全員の

同意が得られていないため、

本章については、非公開

Fig. A5-1. Correlation map between MJ precipitation of mesh grid points around tree-ring site and MJ ERSST data (Smith et al., 2008) from AD 1978 to 2009 (N = 32).

インターネット公表に関する共著者全員の

同意が得られていないため、

本章については、 非公開

Fig. A5-2. Correlation map between May precipitation at Yakushima station and May ERSST data (Smith et al., 2008) from AD 1938 to 2013 (N = 76).

インターネット公表に関する共著者全員の

同意が得られていないため、

本章については、 非公開

Fig. A5-3. Correlation map between May precipitation of the mesh grid points around the tree-ring site and May ERSST data (Smith et al., 2008) from AD 1978 to 2009 (N = 32).

インターネット公表に関する共著者全員の

同意が得られていないため、

本章については、非公開

Fig. A5-4. Correlation map between June precipitation at Yakushima station and June ERSST data (Smith et al., 2008) from AD 1938 to 2013 (N = 76).

インターネット公表に関する共著者全員の

同意が得られていないため、

本章については、非公開

Fig. A5-5. Correlation map between June precipitation of the mesh grid points around the tree-ring site and June ERSST data (Smith et al., 2008) from AD 1978 to 2009 (N = 32).

インターネット公表に関する共著者全員の

同意が得られていないため、

本章については、非公開

Fig. A5-6. Correlation map between July precipitation at Yakushima station and July ERSST data (Smith et al., 2008) from AD 1938 to 2013 (N = 76).

インターネット公表に関する共著者全員の

同意が得られていないため、

本章については、非公開

Fig. A5-7. Correlation map between July precipitation of the mesh grid points around the tree-ring site and July ERSST data (Smith et al., 2008) from AD 1978 to 2009 (N = 32).
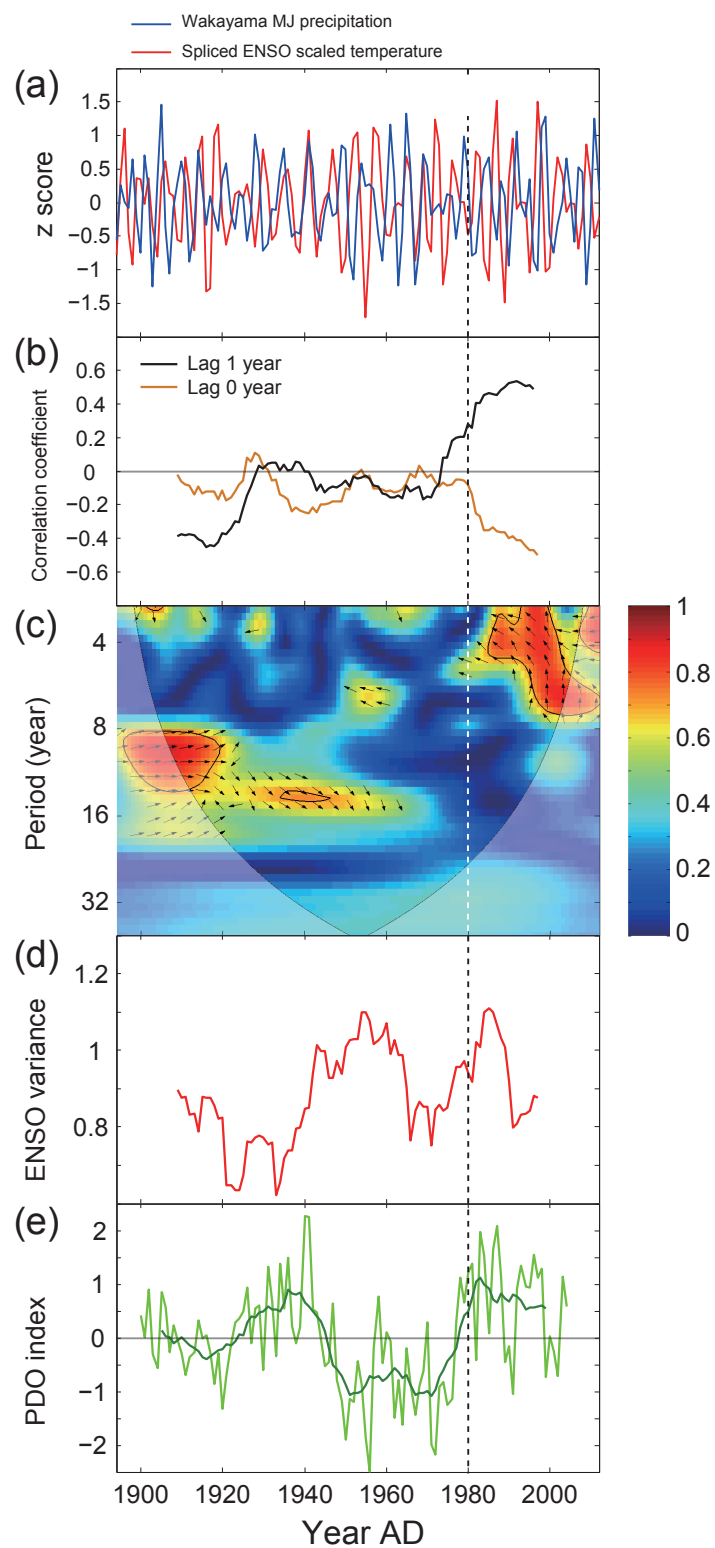
Appendix of chapter 6
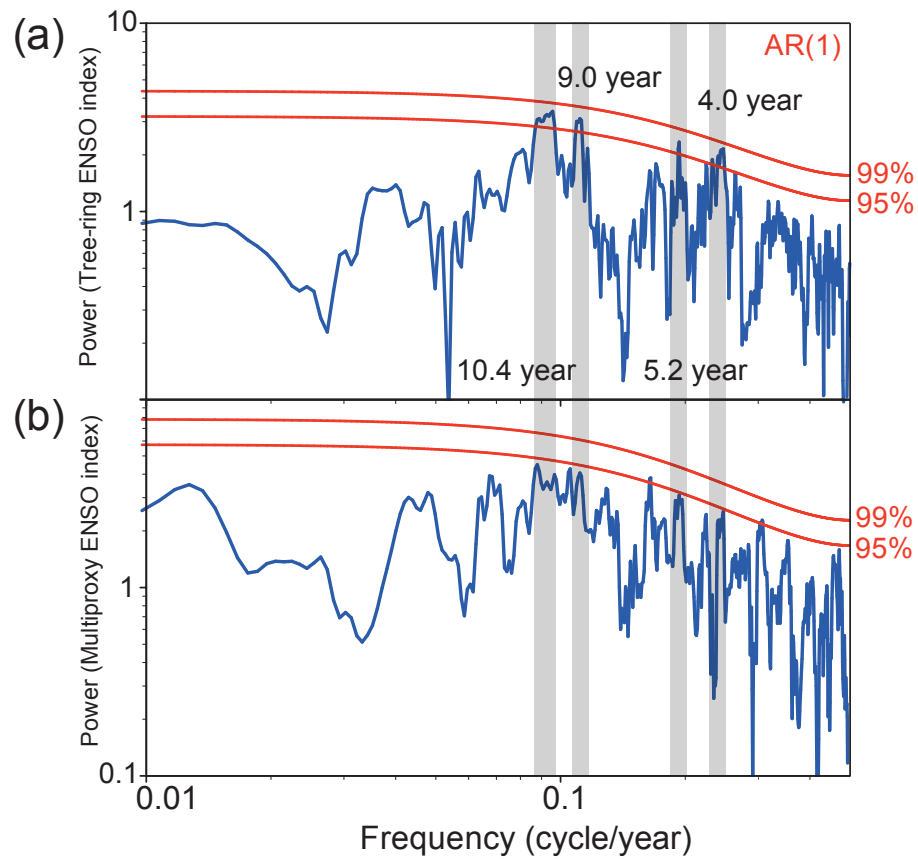
Fig. A6-1. (a) The result of MTM for the tree-ring ENSO reconstruction (Li et al., 2013). (b) The result of MTM for the multiproxy ENSO reconstruction (Braganza et al., 2009). Red solid lines indicate the significant level (95 and 99%).
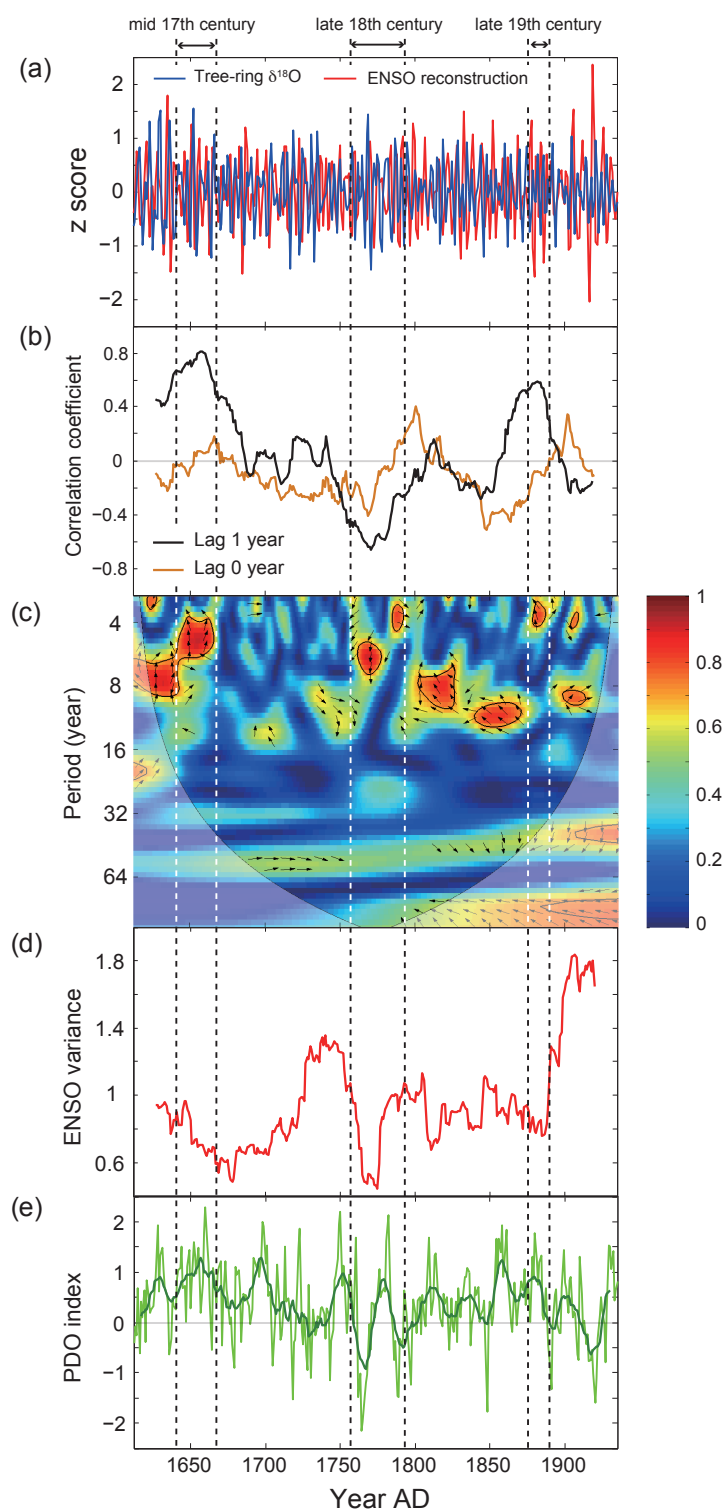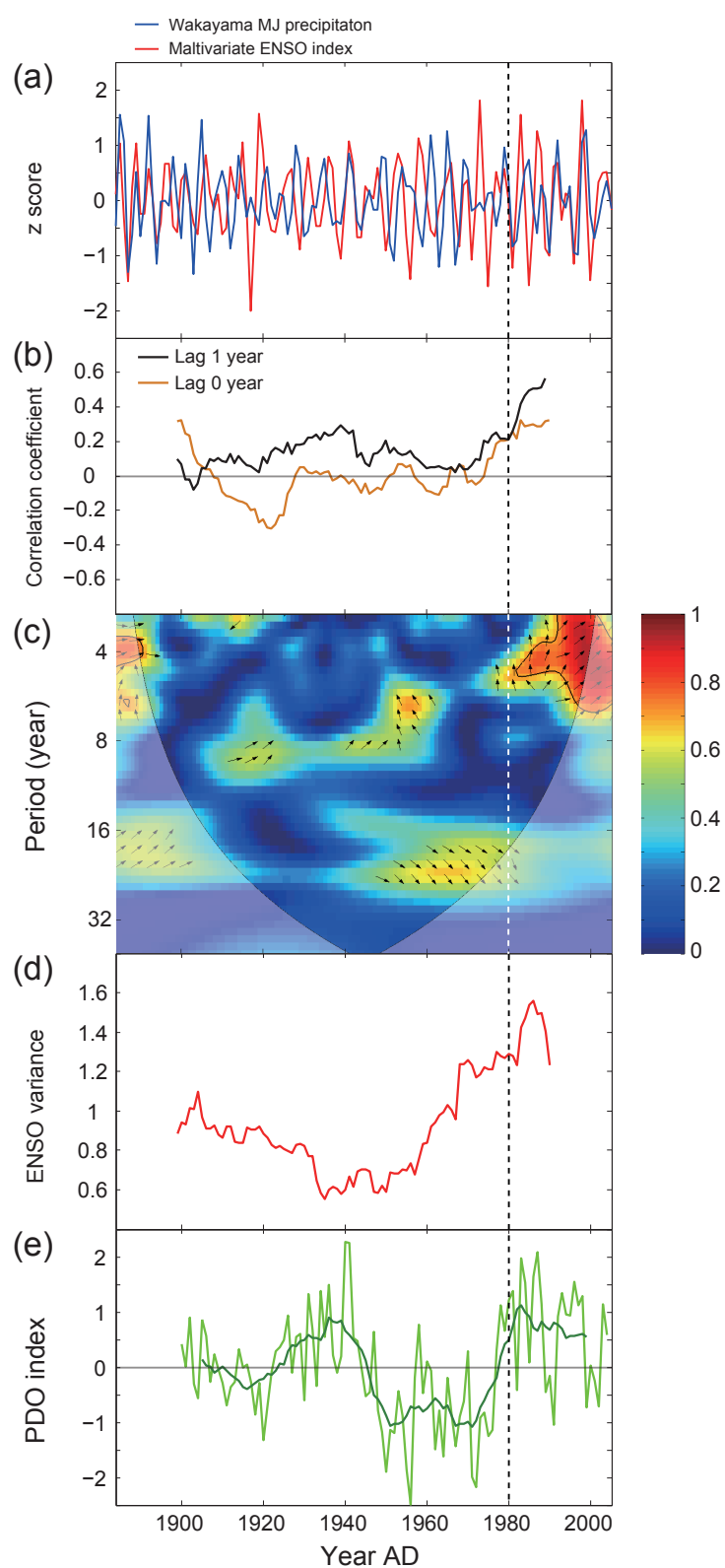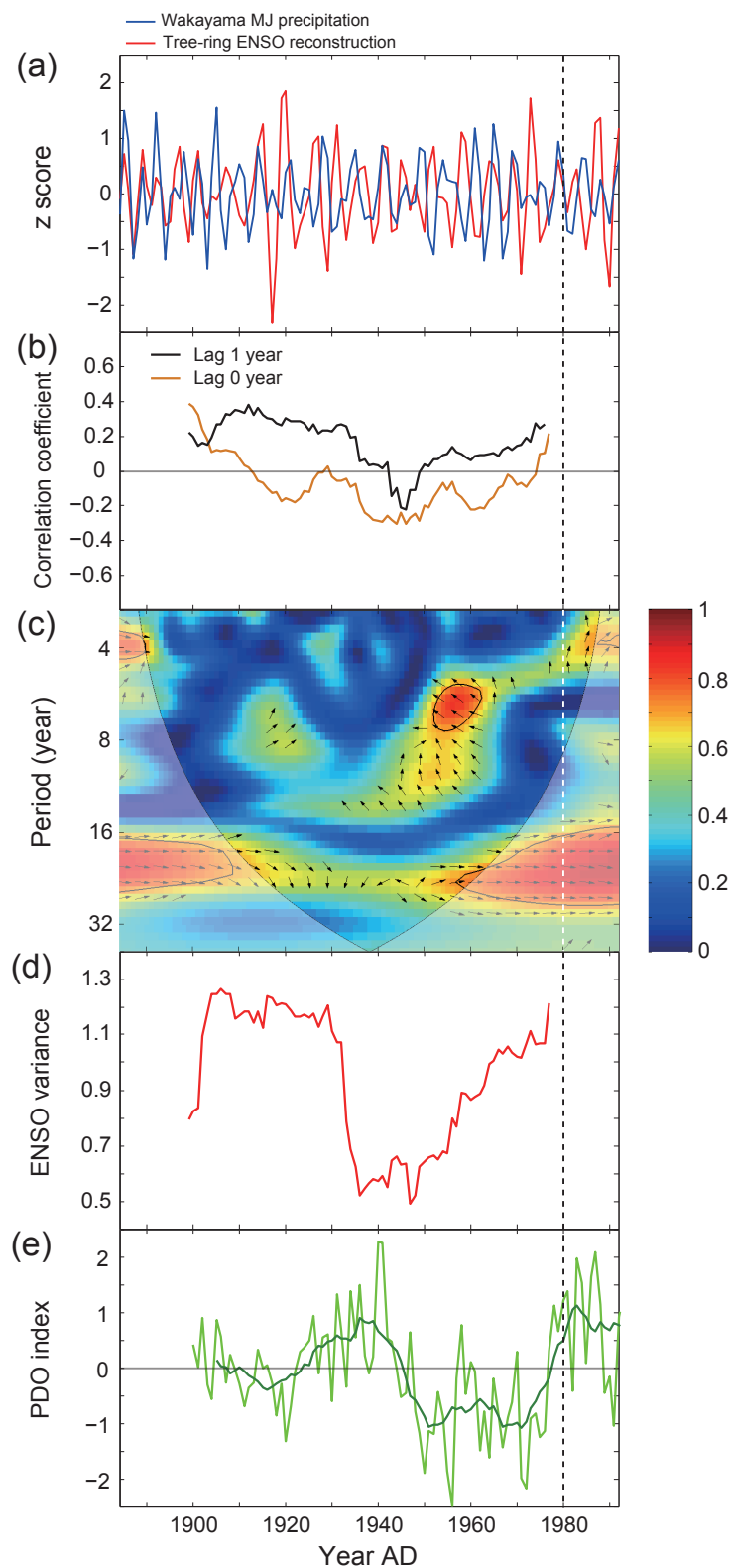
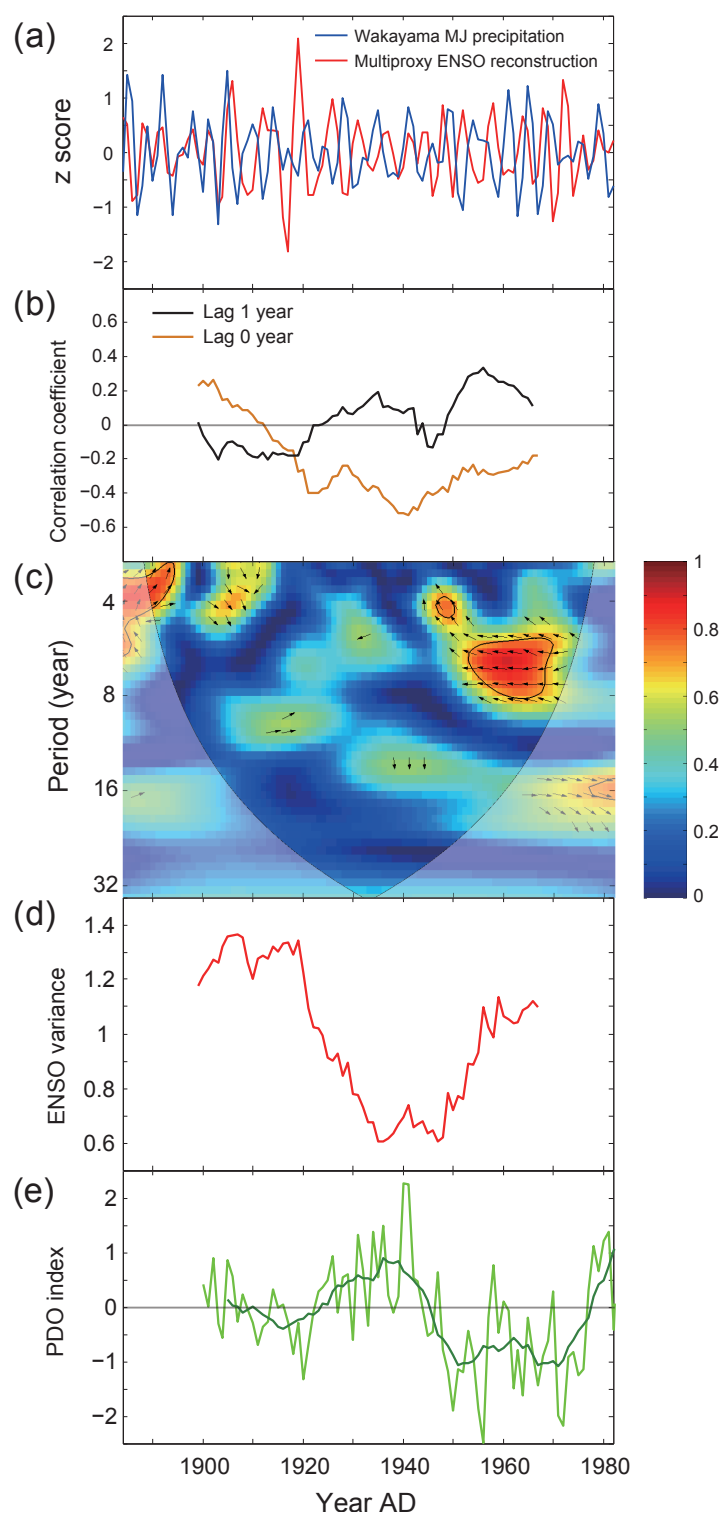**Fig. A6-2.** The same as Fig. 6-1 except for a multiproxy ENSO reconstruction (Braganza et al., 2009).

Fig. A6-3. The same as Fig. 6-2 except for a spliced ENSO scaled temperature (Crowley et al., 2014).

Fig. A6-4. The same as Fig. 6-2 except for a winter (previous December–January) multivariate ENSO index (Wolter and Timlin, 2011).

Fig. A6-5. The same as Fig. 6-2 except for a tree-ring ENSO reconstruction (Li et al., 2013).

Fig. A6-6. The same as Fig. 6-2 except for a multiproxy ENSO reconstruction (Braganza et al., 2009).